

Review

β -Ga₂O₃-Based Heterostructures and Heterojunctions for Power Electronics: A Review of the Recent Advances

Dinusha Herath Mudiyansele ^{1,†} , Bingcheng Da ^{1,†} , Jayashree Adivarahan ¹, Dawei Wang ¹, Ziyi He ¹, Kai Fu ² , Yuji Zhao ³ and Houqiang Fu ^{1,*}

- ¹ School of Electrical, Computer, and Energy Engineering, Arizona State University, Tempe, AZ 85281, USA; dinusha@asu.edu (D.H.M.); bingche1@asu.edu (B.D.); jadivara@asu.edu (J.A.); dwang182@asu.edu (D.W.); ziyihe5@asu.edu (Z.H.)
- ² Department of Electrical and Computer Engineering, The University of Utah, Salt Lake City, UT 84112, USA; kai.fu@utah.edu
- ³ Department of Electrical and Computer Engineering, Rice University, Houston, TX 77005, USA; yuji.zhao@rice.edu
- * Correspondence: houqiang@asu.edu
- † These authors contributed equally to this work.

Abstract: During the past decade, Gallium Oxide (Ga₂O₃) has attracted intensive research interest as an ultra-wide-bandgap (UWBG) semiconductor due to its unique characteristics, such as a large bandgap of 4.5–4.9 eV, a high critical electric field of ~8 MV/cm, and a high Baliga's figure of merit (BFOM). Unipolar β -Ga₂O₃ devices such as Schottky barrier diodes (SBDs) and field-effect transistors (FETs) have been demonstrated. Recently, there has been growing attention toward developing β -Ga₂O₃-based heterostructures and heterojunctions, which is mainly driven by the lack of *p*-type doping and the exploration of multidimensional device architectures to enhance power electronics' performance. This paper will review the most recent advances in β -Ga₂O₃ heterostructures and heterojunctions for power electronics, including NiO_x/ β -Ga₂O₃, β -(Al_xGa_{1-x})₂O₃/ β -Ga₂O₃, and β -Ga₂O₃ heterojunctions/heterostructures with other wide- and ultra-wide-bandgap materials and the integration of two-dimensional (2D) materials with β -Ga₂O₃. Discussions of the deposition, fabrication, and operating principles of these heterostructures and heterojunctions and the associated device performance will be provided. This comprehensive review will serve as a critical reference for researchers engaged in materials science, wide- and ultra-wide-bandgap semiconductors, and power electronics and benefits the future study and development of β -Ga₂O₃-based heterostructures and heterojunctions and associated power electronics.

Keywords: Gallium Oxide; heterostructures; heterojunctions; power electronics



Citation: Herath Mudiyansele, D.; Da, B.; Adivarahan, J.; Wang, D.; He, Z.; Fu, K.; Zhao, Y.; Fu, H. β -Ga₂O₃-Based Heterostructures and Heterojunctions for Power Electronics: A Review of the Recent Advances.

Electronics **2024**, *13*, 1234. <https://doi.org/10.3390/electronics13071234>

Academic Editor: Wojciech Wojtasiak

Received: 24 February 2024

Revised: 20 March 2024

Accepted: 21 March 2024

Published: 27 March 2024



Copyright: © 2024 by the authors. Licensee MDPI, Basel, Switzerland. This article is an open access article distributed under the terms and conditions of the Creative Commons Attribution (CC BY) license (<https://creativecommons.org/licenses/by/4.0/>).

1. Introduction

Although Ga₂O₃ was synthesized over six decades ago, it has remained largely ignored as an ultra-wide-bandgap (UWBG) semiconductor material [1]. It was not until 2011 that Higashiwaki et al. [2] demonstrated its potential by featuring a field-effect transistor (FET) constructed using epitaxially grown β -Ga₂O₃ on bulk Ga₂O₃ single crystals. Shortly thereafter, the potential of Ga₂O₃ was recognized, especially for power electronics, leading to extensive research efforts [3]. These developments are particularly promising for future power electronics. For example, the power electronics industry is projected to play a significant role in providing 80% of the nation's electricity flow by 2030 in the U.S. [4]. This industry will cater to various growing needs, including the expansion of electric vehicles, data centers, renewable energy, consumer electronics, and the space telecommunication sector, with the potential to drastically reduce energy losses in the years to come. The driving force behind this rapid development of β -Ga₂O₃ power devices primarily stemmed from β -Ga₂O₃'s large bandgap of 4.5–4.9 eV, high critical electric field of

~8 MV/cm, impressive Baliga's figure of merit (BFOM) (i.e., ~3000 times larger than that of Si), presence of large native substrates, and controllable *n*-type doping capabilities across a wide range of $\sim 10^{15}$ – 10^{20} cm⁻³ [1–3,5–8]. Ga₂O₃ exists in five polymorphs, with β -Ga₂O₃ being the most thermodynamically stable phase [8]. β -Ga₂O₃ substrates are readily available in sizes up to 4 inches in diameter, and they can be mass-produced using the Edge-Defined Film-Fed Growth (EFG) method [9]. Additionally, high-quality epitaxial layers can be grown on these substrates using various techniques, including halide vapor-phase epitaxy (HVPE) [10], molecular beam epitaxy (MBE) [11], and metal–organic chemical vapor-phase deposition (MOCVD) [12]. Moreover, Ga₂O₃ and its composites can be synthesized using solution-based techniques such as sol-gel [13], hydrothermal [14], and chemical bath methods [15] and electrochemical deposition [16]. These methods enable large-area deposition and a high yield with simple processing at low temperatures in ambient conditions, thereby reducing the complexity and energy consumption during manufacturing. Additionally, these wet chemical solution processes are effective for preparing various types of Ga₂O₃-based nanomaterials [17]. Ga₂O₃ was also investigated for memristors and neuromorphic computing, with resistive switching mechanisms reliant on the formation and dissolution of conductive filaments in a metal–semiconductor–metal (MSM) structure, mainly due to the oxygen vacancies in Ga₂O₃ [18,19]. For *n*-type dopants, the Group IV elements Si, Ge, and Sn form shallow donor states in Ga₂O₃ [20]. The theoretical mobility of β -Ga₂O₃ is ~ 200 cm²/V·s and is primarily limited by interactions with longitudinal optical phonons [21–23]. At low temperatures, a remarkably high carrier mobility exceeding 23,000 cm²/V·s was demonstrated [12]. The saturation velocity of β -Ga₂O₃ is estimated to be 1×10^7 cm/s [24]. β -Ga₂O₃ exhibits a considerably lower thermal conductivity in comparison to other WBG materials such as GaN and SiC [25]. Therefore, effective thermal management stands as an important challenge for the practical use of Ga₂O₃ in power electronic device applications. β -Ga₂O₃ possesses a monoclinic crystal structure with anisotropic physical and electrical properties that vary across different crystallographic orientations [8]. Consequently, attributes such as the dielectric constant [26], thermal conductivity [25], and electron mobility [27] exhibit variations depending on the crystallographic direction. This anisotropy presents both challenges in device fabrication and opportunities for innovative device architectures and operations.

One prominent challenge in the field is the absence of *p*-type β -Ga₂O₃, primarily attributed to significant difficulties in the introduction of acceptor impurities and the generation of holes within the material. Theoretical predictions indicate that the activation energy for acceptors (such as Mg, Zn, Be, and N) in β -Ga₂O₃ is exceptionally high (>1 eV), posing a fundamental hurdle in achieving hole conductivity [28]. Additionally, its flat valence band results in a large effective hole mass, low hole mobility, and a low diffusion constant [29]. To make things worse, holes tend to be localized in β -Ga₂O₃ as small polarons due to lattice distortion rather than behaving as “free” holes [30]. These factors limit the development of electronic devices based on β -Ga₂O₃ and hinder the realization of its full potential as a UWBG semiconductor. Consequently, the majority of the demonstrated β -Ga₂O₃ devices are unipolar, such as FETs [7] and Schottky barrier diodes (SBDs) [31]. Nevertheless, ongoing research endeavors are focused on achieving *p*-type conductivity in β -Ga₂O₃ through methods such as ion implantation [32], co-doping [33], and the formation of heterojunctions with other materials [34]. Heterojunction formation, in particular, has garnered significant attention due to its demonstrated excellent electrical characteristics, including a low on-resistance (R_{on}), a high ON/OFF ratio, and a large reverse blocking voltage [35]. These advances enable further exploration of β -Ga₂O₃'s full potential as a UWBG material, challenging its counterparts like GaN and SiC, where *p*-type doping is available [36,37].

This review primarily focuses on the utilization of β -Ga₂O₃ heterostructures in power electronics applications, which is organized into the following sections. The first section discusses *p*-NiO_x/ β -Ga₂O₃ heterojunctions, which emerge as a viable solution for the lack of *p*-type doping in β -Ga₂O₃ [35]. The second part of the review mainly fo-

cuses on β -(Al_xGa_{1-x})₂O₃/β-Ga₂O₃ heterostructures and their applications in both vertical and lateral devices. The formation of two-dimensional electron gas (2DEG) at the β-(Al_xGa_{1-x})₂O₃/β-Ga₂O₃ heterostructure through Si modulation doping enables the development of modulation-doped FETs (MODFETs). Furthermore, the review explores β-Ga₂O₃ heterostructures and heterojunctions with various other materials for innovative device architectures, including GaN, SiC, SnO, Cu₂O, CuI, and UWBG semiconductors like diamond, aluminum nitride (AlN), and boron nitride (BN). Finally, the discussion extends to β-Ga₂O₃ heterostructures and heterojunctions with two-dimensional (2D) materials like graphene, molybdenum disulfide (MoS₂), tungsten disulfide (WS₂), tungsten diselenide (WSe₂), and black phosphorus (BP). These novel 2D materials possess unique characteristics suitable for diverse device configurations that can achieve efficient carrier transport. This timely review will serve as a valuable reference for the advancement of β-Ga₂O₃-based heterostructures in power electronics applications.

2. *p*-NiO_x/β-Ga₂O₃ Heterojunction

Recently, NiO_x has attracted significant attention as a promising *p*-type material for forming heterojunctions with *n*-type β-Ga₂O₃ [35]. While the incorporation of NiO_x with β-Ga₂O₃ is a relatively recent development, NiO_x has a well-established history of serving as hole contact in solar cell applications [38]. In particular, NiO_x is highly regarded for its efficient extraction of generated holes, notably in perovskite solar cells [39]. Various NiO_x deposition techniques are available, encompassing diverse methods such as sol-gel spin coating [40], RF sputtering [41], plasma-assisted laser deposition [42], electron beam (e-beam) evaporation [43], and the thermal oxidation of Ni [44]. Each of these methods presents its unique advantages and drawbacks. Among these techniques, RF sputtering is the most extensively researched method due to its capability to produce uniform polycrystalline films and control NiO_x doping by adjusting the O₂/Ar gas ratios and deposition pressure. More information about the RF sputtering deposition details can be found elsewhere [41,45,46]. It is important to note, however, that RF sputtering also causes damage to the β-Ga₂O₃ surface, as the high-energy plasma involved can induce interface states that can detrimentally impact the device performance [47]. Nevertheless, it has been demonstrated that sputtering can yield abrupt NiO_x/β-Ga₂O₃ interfaces.

Li et al. [41] and Xia et al. [45] have conducted investigations into the band alignment, bandgap, and resistivity and the influence of the post-annealing temperature on NiO_x films produced via RF magnetron sputtering. Their studies revealed that the bandgap of NiO_x varied from 3.9 to 3.7 eV due to the annealing process, as illustrated in Figure 1a. In Figure 1b, the X-ray photoelectron spectroscopy (XPS) spectrum shows distinct Ni and O peaks. During the deposition process, Ni²⁺ and Ni³⁺ ions can interact with O₂ to form NiO or Ni₂O₃, and the extent of this reaction strongly depends on the O₂/Ar gas flow, as demonstrated in Figure 1d. Figure 1c,f illustrate that annealing led to a reduction in Ni₂O₃ and an increase in NiO, as further confirmed by X-ray diffraction (XRD) measurements. Additionally, it has been observed that the bandgap and resistivity of the films were closely associated with the O₂/Ar gas flow (Figure 1e). Moreover, as described earlier, annealing resulted in a decrease in the bandgap and an increase in the resistivity of the films. Stoichiometric NiO is a wide-bandgap antiferromagnetic insulator [48]. The *p*-type properties of NiO_x primarily arise from the presence of Ni vacancies and O interstitials (native acceptor defects) [49]. NiO_x can also be *p*-type-doped with alkali metals such as Li and K [50]. The elevated O₂ flow during deposition and post-deposition annealing can enhance the stoichiometry of the NiO_x films, resulting in films with a high resistivity and an improved hole mobility. In other words, native acceptor defects are thermally unstable and can be readily eliminated through an annealing process [49]. Furthermore, it has been observed that the polycrystalline nature improved with thermal annealing due to the crystalline grain growth [51].

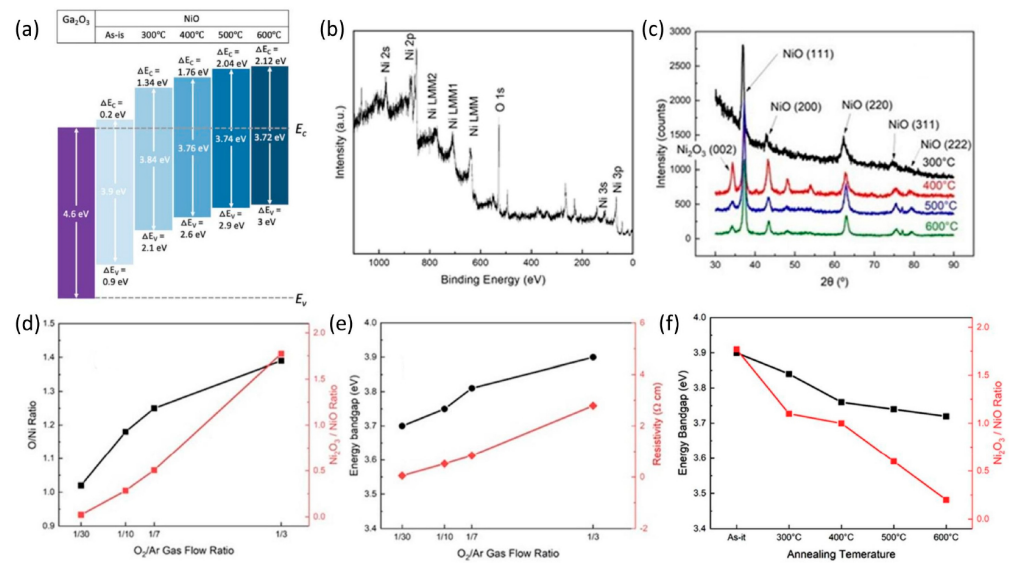


Figure 1. (a) Band alignment of $\text{NiO}_x/\beta\text{-Ga}_2\text{O}_3$ with annealing at varying temperatures (up to 600 °C). (b) X-ray photoelectron spectroscopy (XPS) spectra illustrating the composition of deposited NiO_x . (c) X-ray diffraction (XRD) pattern of NiO_x at different annealing temperatures. (d) Variation in O/Ni and $\text{Ni}_2\text{O}_3/\text{NiO}$ ratios and (e) variation in bandgap and resistivity achieved by changing the O_2/Ar gas flow. (f) Variation in bandgap and $\text{Ni}_2\text{O}_3/\text{NiO}$ ratio with annealing temperature. (a) reproduced with permission from X. Xia et al., *J. Phys. D: Appl. Phys.* 55, 385105 (2022) [45]. Copyright 2022 IOP Publishing. (b–f) reproduced with permission from J.-S. Li et al., *J. Vac. Sci. Technol. A* 41, 013405 (2022) [41]. Copyright 2022 American Vacuum Society.

Kokubun et al. [40] pioneered the development of the first $\text{NiO}_x/\beta\text{-Ga}_2\text{O}_3$ heterostructure with Li-doped $p\text{-NiO}_x$ using a sol-gel spin coating process. While these devices exhibited favorable rectifying behavior, issues such as a high R_{on} and a low breakdown voltage (BV) limited their performance. It was deduced that the prevailing current transport mechanism was attributed to carrier recombination rather than carrier diffusion. Recent reports have further affirmed that, owing to the type-II band alignment of $\text{NiO}_x/\beta\text{-Ga}_2\text{O}_3$ devices, carrier diffusion does not play a significant role under low-bias conditions. Instead, interface recombination (Figure 2a) and multi-step tunneling (Figure 2b) have emerged as the predominant mechanisms governing current transport in these heterojunctions [49,51,52]. Consequently, the quality of the interface holds the utmost importance for such devices. In Figure 2c, a transmission electron microscope (TEM) image of the fabricated $\text{NiO}_x/\beta\text{-Ga}_2\text{O}_3$ diodes is presented, showing Au, Ni, NiO_x , and $\beta\text{-Ga}_2\text{O}_3$ layers. It should be noted that Ni/Au contact acts as good Ohmic contact for NiO_x with the aid of thermal annealing [51]. Figure 2d emphasizes the abrupt nature of the heterojunction using a high-resolution TEM (HRTEM) image; however, it also reveals regions that have incurred damage due to the high-energy plasma involved during sputtering (~ 150 W) [47]. To mitigate such issues, lower-energy plasma (~ 70 W) can be employed for NiO_x deposition, resulting in an abrupt and smooth $\text{NiO}_x/\beta\text{-Ga}_2\text{O}_3$ interface, as depicted in Figure 2e [53]. The damage that occurs during sputtering can introduce interface states that impact the device performance, potentially leading to increased leakage current and degradation of the device functionality. An alternative solution involves the use of e-beam-deposited NiO_x , where the interface quality is improved, as illustrated in Figure 2f [43].

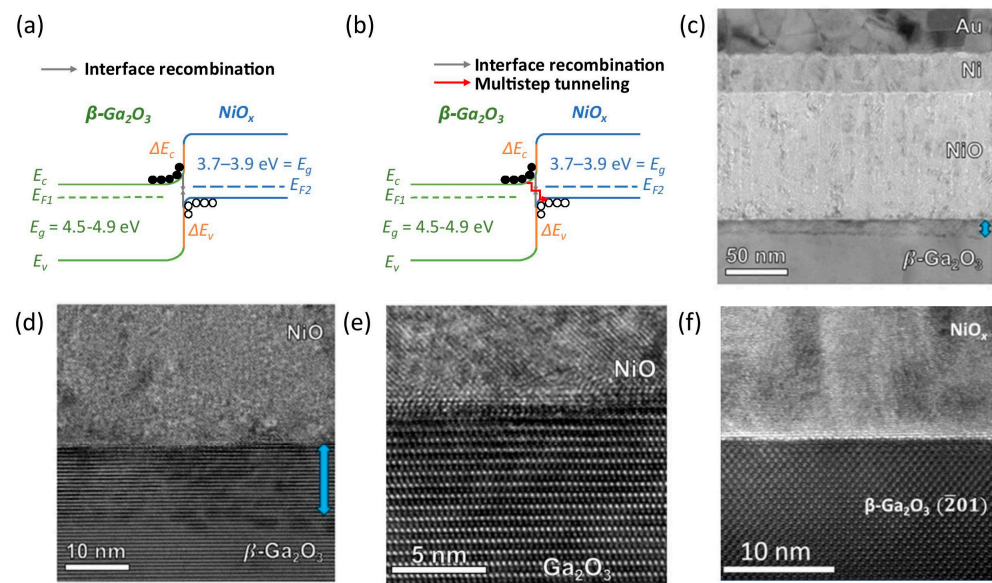


Figure 2. (a) Band alignment and interface recombination at low bias ($< 1.5\text{ V}$) and (b) multi-step tunneling at high bias ($> 1.5\text{ V}$) in a $\text{NiO}_x/\beta\text{-Ga}_2\text{O}_3$ $p\text{-n}$ diode. (c) Transmission electron microscope (TEM) image of a fabricated $p\text{-n}$ diode encompassing all regions. (d) The $p\text{-n}$ diode interface with a sputtered NiO_x layer, with the blue arrow indicating some interface deformation due to the involvement of high-energy plasma (150 W). (e) Low-power sputtered heterojunction with minimal damage to the interface (70 W). (f) E-beam-deposited $p\text{-n}$ diode featuring an abrupt interface. (c,d) reproduced with permission from J.-S. Li et al., *Appl. Phys. Lett.* 121, 042105 (2022) [47]. Copyright 2022 AIP Publishing. (e) reproduced with permission from J.-S. Li et al., *Crystals (Basel)* 13, 886 (2023) [53]. Copyright 2023 under the terms of CC BY 4.0. (f) reproduced with permission from D. H. Mudiyansele et al., *Appl. Phys. Express* 16, 094002 (2023) [43]. Copyright 2023 IOP Publishing.

The anisotropic nature of $\text{NiO}_x/\beta\text{-Ga}_2\text{O}_3$ in different crystal orientations has also been investigated. Deng et al. [54] investigated the dependence of the band alignment of $\text{NiO}_x/\beta\text{-Ga}_2\text{O}_3$ heterostructures on various crystal orientations and revealed differences in the conduction and valence band offsets. Specifically, (−201) exhibited the lowest conduction and highest valence band offsets, while (010) showed the opposite trend. Subsequent investigations involved the use of e-beam-evaporated NiO_x in various $\beta\text{-Ga}_2\text{O}_3$ crystal orientations, confirming clear interfaces across different orientations through HRTEM studies [43]. However, a significant disparity in the electronic properties was observed between (−201) [or (001)] and (010) orientations, manifesting as variations in the turn-on voltage, ON/OFF ratio, interface defect density, and temperature-dependent forward current transport. These differences are primarily attributed to distinct atomic configurations, the density of the dangling bonds, and variations in the interface trap-state densities across different crystal planes [43]. $\text{NiO}_x/\beta\text{-Ga}_2\text{O}_3$ heterostructures commonly exhibit hysteresis, attributed to the interface traps at the $\text{NiO}_x/\beta\text{-Ga}_2\text{O}_3$ heterojunction. Hao et al. [55] demonstrated a reduction in I–V hysteresis by subjecting the devices to $350\text{ }^\circ\text{C}$ thermal annealing for 3 min post-fabrication. This annealing process resulted in a decrease in the interface trap states from 1.04×10^{12} to $1.33 \times 10^{11}\text{ eV}^{-1}\text{cm}^{-2}$ and a reduction in the ideality factor from 3.02 to 1.27 after annealing. Following optimization, the devices achieved a BV of 1.63 kV with a high power figure of merit (PFOM) of 0.65 GW/cm^2 . Gong et al. [52] and Yan et al. [56] investigated interface trap states using capacitance–frequency (C–F) measurements and fitted the data with equations that assumed the distribution of the interface states into two energy states. The use of two states proved more effective, representing the interface states closer to the conduction band and others with deeper energy levels [43]. Gong et al. [52] and Yan et al. [56] both observed interface states in the order of $\sim 10^{10}\text{ eV}^{-1}\text{cm}^{-2}$, which are among the lowest reported values. In addition,

Li et al. [57] demonstrated the thermal annealing stability of NiO_x/β-Ga₂O₃ *p-n* diodes from 300 to 500 °C in comparison with the as-deposited NiO_x/β-Ga₂O₃ *p-n* diodes. Annealing at 300 °C resulted in a reduced low forward bias current, while the specific on-resistance ($R_{on,sp}$) remained relatively stable. However, annealing at higher temperatures from 400 to 500 °C degraded the $R_{on,sp}$ due to the increased resistivity of the NiO_x and degraded Ni/Au contact. Between 300 and 500 °C, the reverse leakage current decreased compared to in the as-deposited samples, with the 300 °C annealed sample exhibiting the highest BV. This indicates that temperature optimization is crucial to enhancing the heterointerface in these devices.

Lu et al. [58] demonstrated a NiO_x/β-Ga₂O₃ heterojunction *p-n* diode with a low $R_{on,sp}$ of 3.5 mΩ·cm² and a high BV of 1.06 kV. A low reverse leakage of <1 μA/cm² was observed until its breakdown. Zhang et al. [59] showcased a *p-n* diode featuring an impressive BV of 8.32 kV and an $R_{on,sp}$ of 5.24 mΩ·cm², resulting in a PFOM of 13.2 GW/cm². In Figure 3a, the device configuration is depicted, featuring two NiO_x regions and a field plate (FP) structure designed to withstand high BVs. Utilizing a double NiO_x layer provided a low $R_{on,sp}$ for the device while maintaining the BV [49]. The devices had drift regions of 7.5 and 13 μm with an unintentional doping (UID) concentration of 5–7 × 10¹⁵ cm⁻³. Figure 3b illustrates the forward I–V characteristics and $R_{on,sp}$ curves for both device types. Additionally, these devices exhibited remarkable thermal stability up to 150 °C, as indicated in Figure 3c. Figure 3d presents the BV curves for these devices, marking a significant milestone in the NiO_x/β-Ga₂O₃ *p-n* diode research. Li et al. [47] presented a noteworthy achievement with a 4.7 kV NiO_x/β-Ga₂O₃ *p-n* diode through meticulous optimization of the thickness of the lower NiO_x layer. Their device fabrication process aligned with the TCAD simulations, which indicated that extending the NiO_x layer beyond the contact area could effectively alleviate electric field crowding, ultimately leading to a high BV. In Figure 3e, the device structure is depicted, while Figure 3f illustrates the forward I–V curves for the fabricated devices with varying thicknesses of the lower NiO_x layer in comparison to a conventional β-Ga₂O₃ SBD. Figure 3g showcases the corresponding BVs, and Figure 3h presents the forward I–V curves in log scale, along with a comparison of the $R_{on,sp}$ of the devices. These devices showed a notable PFOM of 2 GW/cm². The same authors conducted a comprehensive study to optimize the NiO_x doping, thickness, and junction termination extension (JTE) for NiO_x/β-Ga₂O₃ devices with kV-class operation using Silvaco TCAD simulations [60]. Additionally, they successfully demonstrated high-BV devices with a maximum of 6.5 kV, achieved through thermal annealing optimization [57]. They also showcased *p-n* diodes with a 3.6 kV BV and a 4.8 A current capability within a 1 mm² device area [61].

Xiao et al. [62] demonstrated a ~3.5 kV NiO_x/β-Ga₂O₃ *p-n* diode with multiple JTEs of NiO_x layers with different lengths (Figure 4a). This mechanism allows a gradual decrease in the effective charge carriers away from the device's active region to smoothen the electric field crowding at the anode edge, as in Figure 4b. The bottom two JTEs consisted of lightly doped NiO_x, while the top JTE was highly doped. This structure reduces the crowded electric field at the anode by reducing the surface electric field. Figure 4c shows the BV of devices with JTEs fabricated on two sets of wafers and without JTEs. Zhou et al. [63] presented a *p-n* diode featuring a bevel structure, as shown in Figure 4d, which exhibited remarkable characteristics, including a high BV of 2.04 kV and an impressive $R_{on,sp}$ of 2.26 mΩ·cm². These devices demonstrated a significant BFOM of 1.84 GW/cm² (2.87 GW/cm²) with DC (pulsed) measurements. In Figure 4e, the BV curves of these diodes compared to a conventional β-Ga₂O₃ SBD with and without bevel edge termination are depicted. Figure 4f illustrates an effective reduction in electric field crowding using various bevel angles. Furthermore, this device exhibited a rapid reverse recovery time of 16.4 ns, outperforming Si fast-recovery diodes (Si FRDs), showing a significant advancement in current technology (Figure 4g). Hao et al. [64] demonstrated a 2.6 kV *p-n* diode by employing a JTE and annealing the device at 300 °C for 10 min. This diode exhibited stability at high temperatures and a BV of 1.77 kV at 250 °C. Furthermore, a low

$R_{on,sp}$ of $2.5 \text{ m}\Omega\cdot\text{cm}^2$ resulted in a PFOM of $2.83 \text{ GW}/\text{cm}^2$. Wang et al. [65] achieved a $2.41 \text{ kV } p\text{-}n$ diode with a JTE and a small-angle beveled FP, boasting a remarkable $R_{on,sp}$ of $1.12 \text{ m}\Omega\cdot\text{cm}^2$ and a record BFOM of $5.18 \text{ GW}/\text{cm}^2$. Gong et al. [66] demonstrated a $1.86 \text{ kV NiO}_x/\beta\text{-Ga}_2\text{O}_3$ $p\text{-}n$ diode that showed stability at 400 K with the use of double NiO_x layers. Most recently, a $\text{NiO}_x/\beta\text{-Ga}_2\text{O}_3$ $p\text{-}n$ diode with a 7.5 kV BV , a PFOM of $6.2 \text{ GW}/\text{cm}^2$, and an ON/OFF ratio of $>10^{13}$ was demonstrated [67]. Collectively, these works highlight the immense potential of $p\text{-NiO}_x/\beta\text{-Ga}_2\text{O}_3$ heterojunctions for advanced power device applications.

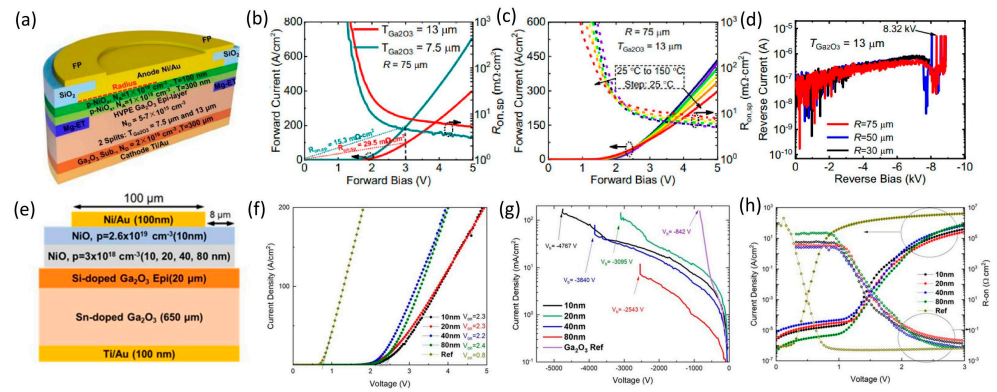


Figure 3. (a) A $p\text{-}n$ diode with an 8.32 kV BV . (b) Forward I-V and $R_{on,sp}$ of devices with 7.5 and $13 \mu\text{m}$ drift layers. (c) Temperature-dependent forward I-V and $R_{on,sp}$. (d) Reverse BV curve of the device with a $13 \mu\text{m}$ drift layer with different-diameter Ohmic contacts. (e) A $4.7 \text{ kV BV } p\text{-}n$ diode. (f) Forward I-V and (g) reverse BV of demonstrated devices. (h) Forward I-V and $R_{on,sp}$ on log scale. (a–d) reproduced with permission from J. Zhang et al., *Nat. Commun.* 13, 3900 (2022) [59]. Copyright 2022 under the terms of CC BY 4.0. (e–h) reproduced with permission from J.-S. Li et al., *Appl. Phys. Lett.* 121, 042105 (2022) [47]. Copyright 2022 AIP Publishing.

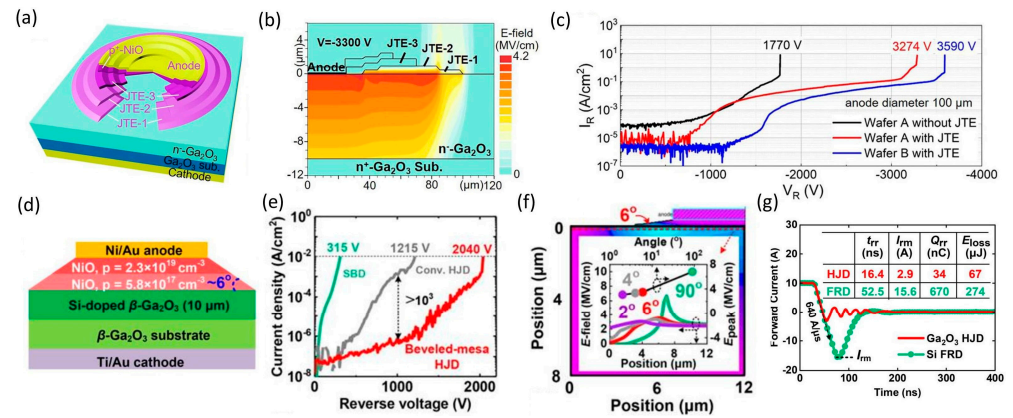


Figure 4. (a) A $\text{NiO}_x/\beta\text{-Ga}_2\text{O}_3$ $p\text{-}n$ diode with multiple JTEs of various lengths. (b) Electric field profile of the device with 3.3 kV reverse bias. (c) BV curves of devices with and without JTEs. (d) A $2.04 \text{ kV } p\text{-}n$ diode with beveled mesa edge termination. (e) BV comparison of SBD, heterojunction diode, and beveled mesa heterojunction diode. (f) Simulation of and reduction in electric field crowding with bevel angle. (g) Comparison of reverse recovery curves of $\text{NiO}_x/\beta\text{-Ga}_2\text{O}_3$ heterojunction and Si FRD. (a–c) reproduced with permission from M. Xiao et al., *Appl. Phys. Lett.* 122, 183501 (2023) [62]. Copyright 2023 AIP Publishing. (d–g) F. Zhou et al., *Appl. Phys. Lett.* 119, 262103 (2021) [63]. Copyright 2021 AIP Publishing.

In addition to $p\text{-}n$ junctions, NiO_x can serve as a material for edge termination in $\beta\text{-Ga}_2\text{O}_3$ devices. This facilitates charge balance at the heterojunction, reducing electric field crowding and enhancing the device’s high-voltage-handling capabilities. NiO_x -based JTEs [56,62,68], guard rings [69], and reduced surface field structures (RESURFs) [70,71]

have been reported as edge terminations for β -Ga₂O₃ devices. Yan et al. [56] demonstrated a β -Ga₂O₃ SBD with NiO_x heterojunction edge termination and a SiO₂ FP structure (Figure 5a). These devices showed an average BV of 1.86 kV and an $R_{on,sp}$ of 3.12 m Ω ·cm², yielding a BFOM of 1.11 GW/cm². Furthermore, these devices showed a low interface trap density of 4.13×10^{10} eV⁻¹cm⁻². Figure 5b–d show the forward I–V, $R_{on,sp}$, and BV of SBDs with different anode diameters. Gong et al. [69] showcased a high-performance SBD with *p*-NiO_x field-limiting rings (FLRs). A BFOM of 0.46 GW/cm² was obtained with a 1.89 kV BV and an $R_{on,sp}$ of 7.7 m Ω ·cm² for an SBD with an FLR width/spacing of 2 μ m. It should be noted that an 8 μ m JTE is also included in the design before the FLRs, as in Figure 5e. In this work, the authors fabricated *p*-*n* diodes, junction barrier Schottky diodes (JBS), conventional SBDs, and SBDs with 2 and 3 μ m FLRs. Figure 5f–h show the forward I–V, $R_{on,sp}$, and BV of all the fabricated devices. Wang et al. [68] presented an SBD with three JTEs stacked on top of each other. These JTEs served to inhibit the electric field crowding in proximity to the Schottky contact, thus facilitating efficient charge extraction during device switching. Ma et al. [46] demonstrated the control of *p*-type doping in NiO_x in the range of $<10^{18}$ to 2×10^{18} cm⁻³ by changing the O₂ partial pressure during RF magnetron sputtering. Precise control of *p*-type doping allows for charge balance in the *n*-type Ga₂O₃ region, leading to SBDs with ~ 8 kV BV. Recently, Qing et al. [71] presented an SBD featuring a NiO_x RESURF structure that achieves a BV exceeding 10 kV, both at room temperature and 200 °C. Achieving a 10 kV performance at both room temperature and 200 °C marks a significant milestone in power electronics, highlighting the substantial potential of NiO_x/ β -Ga₂O₃ devices.

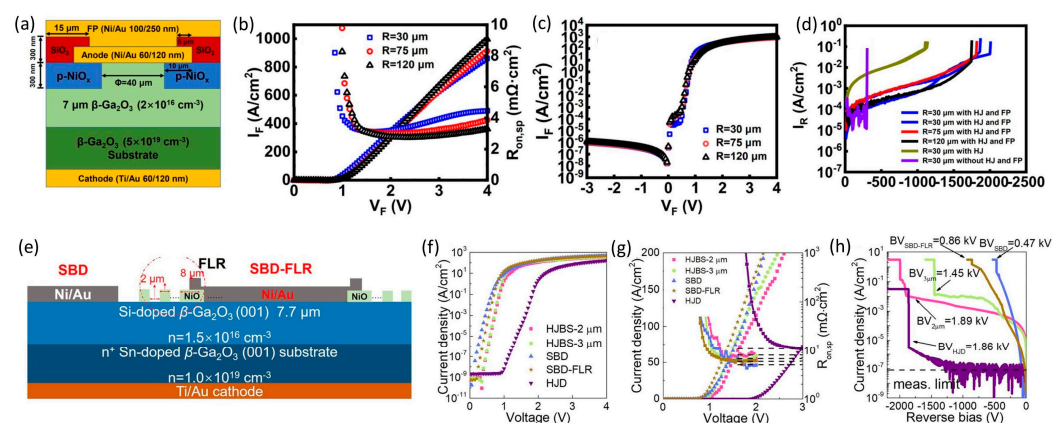


Figure 5. (a) β -Ga₂O₃ SBD with a *p*-NiO_x heterojunction edge termination and SiO₂ FP. (b) Forward I–V and $R_{on,sp}$ of devices with different diameters. (c) Forward I–V on log scale. (d) BV curves of devices with and without heterojunction and FP. (e) Schematic of SBD with and without FLRs. (f) Forward I–V of JBS, SBD, and SBD-FLR devices on a log scale. (g) Forward I–V on a linear scale and $R_{on,sp}$ of devices. (h) BV curves of all demonstrated devices. (a–d) reproduced with permission from Q. Yan et al., *Appl. Phys. Lett.* 120, 092106 (2022) [56]. Copyright 2022 AIP Publishing. (e–h) H. H. Gong et al., *Appl. Phys. Lett.* 118, 202102 (2021) [69]. Copyright 2021 AIP Publishing.

The JBS diodes combine the advantages of both SBDs and *p*-*n* diodes, offering the low turn-on voltage of SBDs and the low reverse leakage current of *p*-*n* diodes. During forward bias conditions, the Schottky regions are activated, allowing for efficient high-current transport, while at reverse bias, the Schottky regions were shielded from a high electric field due to the potential barrier from the *p*-*n* junction regions. Therefore, JBS devices have reduced resistive losses during forward bias (low turn-on) and the capability to handle high blocking voltages during reverse bias. The availability of *p*-type NiO_x enables the fabrication of NiO_x/ β -Ga₂O₃ JBS diodes. Multiple JBS diodes have been successfully demonstrated to have the capability for high forward currents and high reverse blocking voltages, some reaching into the kV-class [72–74]. These achievements were made possible through the utilization of sputtered and thermally oxidized *p*-NiO_x. Lv et al. [72] showed a

JBS diode featuring an $R_{on,sp}$ of $3.45 \text{ m}\Omega\cdot\text{cm}^2$, along with a BV of 1.75 kV for a small-area device ($100 \mu\text{m}^2$). This small-area device exhibited an impressive BFOM of $0.85 \text{ GW}/\text{cm}^2$. For a larger-area device (1 mm^2), it delivered 5 A of forward current and could withstand voltages up to $\sim 0.7 \text{ kV}$. The NiO_x was obtained through thermal oxidation, involving the exposure of a 5 nm Ni layer to a temperature of $600 \text{ }^\circ\text{C}$ for a duration of 10 min in an O_2 atmosphere. In the resulting devices, SBD exhibited a turn-on voltage of 0.7 V, while the JBS diode had a slightly higher turn-on voltage of 1.0 V. This slight difference in voltage is due to the lateral depletion of the $\text{NiO}_x/\beta\text{-Ga}_2\text{O}_3$ heterojunctions in the JBS diode. Yan et al. [73] reported a JBS diode with an $R_{on,sp}$ of $1.94 \text{ m}\Omega\cdot\text{cm}^2$ and a BV of 1.34 kV, resulting in a PFOM of $0.93 \text{ GW}/\text{cm}^2$. The reduction in the $\beta\text{-Ga}_2\text{O}_3$ fin width was identified as a contributing factor to minimizing the reverse leakage current due to the enhanced sidewall depletion in the $p\text{-NiO}_x$. The devices were manufactured using sputtered NiO_x and varying $\beta\text{-Ga}_2\text{O}_3$ fin widths, specifically 1.5, 3, and $5 \mu\text{m}$. Wu et al. [74] presented a JBS diode with and without a beveled FP. The incorporation of a beveled FP effectively reduced the electric field crowding from 7.8 to $5.1 \text{ MV}/\text{cm}$. These JBS diodes exhibited a di/dt of $\sim 400 \text{ A}/\mu\text{s}$, a reverse recovery time of 26.8 ns, and a reverse recovery charge of 46.2 nC. Additionally, these devices were assembled and used to construct a voltage multiplier, demonstrating the practical applicability of $\text{NiO}_x/\beta\text{-Ga}_2\text{O}_3$ JBS diodes. These results highlight the promising future of $\text{NiO}_x/\beta\text{-Ga}_2\text{O}_3$ JBS diodes for high-current, high-voltage applications, paving the way for energy-efficient power electronics.

Over the years, $\beta\text{-Ga}_2\text{O}_3$ -based lateral FETs have shown significant advancements in their electrical properties [7]. However, to approach the material's limits with $\beta\text{-Ga}_2\text{O}_3$, achieving a lower R_{on} and a higher BV is imperative. Introducing NiO_x beneath the gate in $\beta\text{-Ga}_2\text{O}_3$ -based lateral FETs can enhance the R_{on} and improve the breakdown characteristics. This innovative configuration is referred to as a $\text{NiO}_x/\beta\text{-Ga}_2\text{O}_3$ -based junction field-effect transistor (JFET). In lateral FETs, higher channel doping can lead to a lower R_{on} , but it may also decrease the device's BV. However, by incorporating NiO_x under the gate, vertical depletion within $\beta\text{-Ga}_2\text{O}_3$ can allow for higher doping to optimize the R_{on} without compromising the device's BV. Moreover, lateral depletion can reduce the electric field crowding on the drain side of the gate, further enhancing the device's BV. Wang et al. [75] introduced the first $\text{NiO}_x/\beta\text{-Ga}_2\text{O}_3$ JFET. The output and transfer characteristics of the devices feature an R_{on} of $38 \text{ m}\Omega\cdot\text{mm}$ and an ON/OFF ratio of 10^{10} . The device exhibited a subthreshold slope (SS) of $76 \text{ mV}/\text{Dec}$ and a BV of 1.12 kV. Zhou et al. [76] presented a normally-off $\text{NiO}_x/\beta\text{-Ga}_2\text{O}_3$ JFET with a recessed gate and a NiO_x layer. This device exhibited a threshold voltage (V_{th}) of 0.9 V, an R_{on} of $151.5 \Omega\cdot\text{mm}$, a BV of 0.98 kV, and a SS of $73 \text{ mV}/\text{Dec}$. These results indicate promising early developments for $\text{NiO}_x/\beta\text{-Ga}_2\text{O}_3$ JFETs.

Recent advancements in $\text{NiO}_x/\beta\text{-Ga}_2\text{O}_3$ heterojunction devices showcase their remarkable potential in high-voltage and high-power applications. These innovations encompass kV-class $p\text{-n}$ diodes, NiO_x edge-terminated Ga_2O_3 SBDs, JBS diodes, and JFETs. These devices offer enhanced electrical characteristics and exhibit impressive voltage handling capabilities ranging from ~ 1 to 10 kV. It is worth noting that even though p -type doping of $\beta\text{-Ga}_2\text{O}_3$ might be realized in the future, heterojunction $p\text{-n}$ diodes still present some advantages over homojunction $p\text{-n}$ diodes. Heterojunction diodes allow for tuning of the electronic properties based on the conduction and valence band offsets, which offers unique device characteristics, such as fast switching. Moreover, heterojunctions offer a cost-effective approach to device processing and enable advanced device designs that homojunction devices struggle to achieve. These remarkable advancements highlight the substantial progress made in the application of $\text{NiO}_x/\beta\text{-Ga}_2\text{O}_3$ heterojunction devices, setting the stage for more energy-efficient and high-performance power electronics that are well suited to meet the demands of the next decade.

3. β -(Al_xGa_{1-x})₂O₃/β-Ga₂O₃ Heterostructures

Alloying Ga₂O₃ with Al₂O₃ results in (Al_xGa_{1-x})₂O₃ [77], which possesses an increased bandgap (e.g., 4.8–6.2 eV for $x = 0$ to 0.71) [78]. β -(Al_xGa_{1-x})₂O₃ represents a monoclinic ternary alloy expected to offer a higher BFOM than β -Ga₂O₃, rendering it more suitable for power electronics applications [77]. A significant challenge lies in the production of high-quality β -(Al_xGa_{1-x})₂O₃ layers with a substantial Al content, such as exceeding 20% in (010) β -Ga₂O₃ substrates [79]. This challenge arises from the fact that β -Ga₂O₃ has a monoclinic crystalline structure, while Al₂O₃ tends to adopt a corundum structure, leading to phase separation with a high Al content [80]. Additionally, the lattice mismatch with a high Al composition makes the epitaxial growth of β -(Al_xGa_{1-x})₂O₃ on β -Ga₂O₃ a particularly demanding task. The primary approaches to growing β -(Al_xGa_{1-x})₂O₃ are MBE [1] and MOCVD [78]. It is worth noting that other methods, such as pulsed laser deposition (PLD) [81] and sputtering [82], can also be employed for depositing β -(Al_xGa_{1-x})₂O₃. This section primarily focuses on β -(Al_xGa_{1-x})₂O₃/β-Ga₂O₃ heterostructures grown using MBE and MOCVD for power electronics.

Oshima et al. [83] presented the early stages of β -(Al_xGa_{1-x})₂O₃/β-Ga₂O₃ growth using plasma-assisted MBE (PAMBE) on (100) β -Ga₂O₃ single crystals grown via the floating zone (FZ) method. During PAMBE growth, Ga and Al were evaporated from the effusion cells within RF-generated O plasma, resulting in the formation of β -(Al_xGa_{1-x})₂O₃ thin films. More detailed growth parameters are provided elsewhere [76,77]. The Al content in the grown films was estimated by analyzing the shift in the high-resolution X-ray diffraction (HRXRD) spectra between the β -Ga₂O₃ and β -(Al_xGa_{1-x})₂O₃ (020) peaks [84]. Using the equation $x = 0.4727 \times \Delta\theta_{020}$, the Al composition in the (010) crystal orientations could be accurately determined, where $\Delta\theta_{020}$ represents the shift between the β -Ga₂O₃ and β -(Al_xGa_{1-x})₂O₃ (020) peaks. They successfully incorporated Al up to $x = 0.61$ while maintaining the integrity of the β -phase crystal structure. However, at $x = 0.68$, the sample became polycrystalline, and the surface roughness of the samples was high. Stephen et al. [85] demonstrated the growth of β -(Al_xGa_{1-x})₂O₃/β-Ga₂O₃ in (010) crystal orientations with a varying Al content in the range of $x = 0.1$ to 0.18 by optimizing the PAMBE growth conditions, such as substrate temperature and Al flux. These samples showed a good surface morphology with a maximum incorporation of 18% Al.

Zhang et al. [86] demonstrated a two-dimensional electron gas (2DEG) with high electron mobility through modulation doping and the use of Fe-doped semi-insulating β -Ga₂O₃ substrates. In the band diagram of β -(Al_xGa_{1-x})₂O₃/β-Ga₂O₃, the Fermi level is above the conduction band (Figure 6c), leading to carrier accumulation at the interface. The β -(Al_xGa_{1-x})₂O₃ layer can be modulation-doped with Si (δ -doping) (Figure 6a), and these free carriers migrate to the interface, resulting in the formation of a 2DEG with a sheet electron density of approximately 10^{12} cm⁻². Figure 6b displays the HRXRD spectra of the grown β -(Al_xGa_{1-x})₂O₃/β-Ga₂O₃ heterostructures. Two samples were grown with 130 and 360 nm buffer layers. The thicker buffer layer exhibited a higher 2DEG density due to the reduction in the backside depletion. Hall measurements were done using the van der Pauw geometry of the regrown highly doped β -Ga₂O₃ contact, and the charge density showed a weak temperature dependence (Figure 6d), indicating the presence of a formed 2DEG channel with a high low-temperature mobility of 2790 cm²/V·s at 50 K. The room temperature mobility was measured at 162 cm²/V·s for sample A and 180 cm²/V·s for sample B. The observed mobility was fitted using models for polar optical phonon scattering, remote impurity scattering, background impurity scattering, interface roughness scattering, and acoustic deformation potential scattering. A good agreement between the experimental values and fitting was observed, as demonstrated in Figure 6e,f. These findings demonstrate the formation of a 2DEG channel using β -(Al_xGa_{1-x})₂O₃/β-Ga₂O₃ with Si modulation doping.

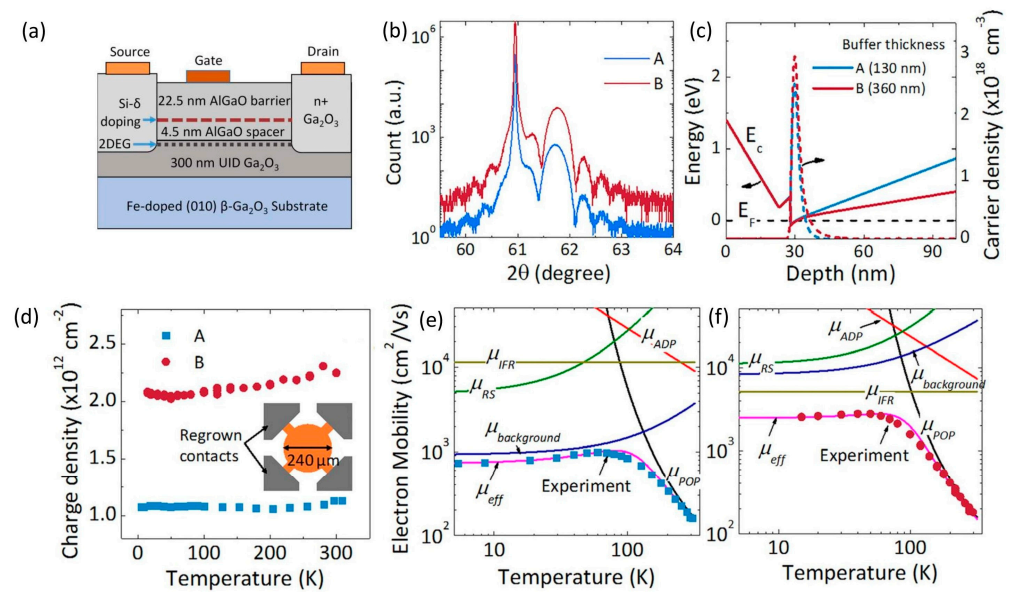


Figure 6. (a) A modulation-doped FET (MODFET) grown using MBE with Si modulation doping (δ -doping). (b) The HRXRD spectra of the grown films A and B. (c) A band diagram of the heterostructure and confinement of 2DEG. (d) The carrier density vs. temperature from Hall measurements. The measured and fitted mobility in samples (e) A and (f) B. (a–f) reproduced with permission from Y. Zhang et al., *Appl. Phys. Lett.* 112, 173502 (2018) [86]. Copyright 2018 AIP Publishing.

Miller et al. [87] reported the MOCVD growth of β -(Al_xGa_{1-x})₂O₃/β-Ga₂O₃ using the metal–organic precursors trimethylaluminum (TMAI) and triethylaluminium (TEAL) as the Al source and triethylgallium (TEGa) as the Ga source and O₂ for oxidation. They successfully achieved β -(Al_xGa_{1-x})₂O₃ alloys with an Al content x up to 43% on sapphire substrates and demonstrated β -(Al_xGa_{1-x})₂O₃/β-Ga₂O₃ superlattices. Compared to MBE, MOCVD is the industrial standard tool for the mass production of epitaxial compound semiconductor films. However, MBE operates under an ultra-high vacuum and requires the substrate temperature to be kept at <700 °C to reduce the decomposition of Ga₂O₃ into volatile suboxides. This limits the maximum Al₂O₃ incorporation into β-Ga₂O₃ to around 25% using MBE [88]. In contrast, the low to medium pressure in MOCVD allows the growth of β -(Al_xGa_{1-x})₂O₃ at substrate temperatures >800 °C, with high solubility of the Al₂O₃ in β-Ga₂O₃. This prevents the formation of volatile suboxides and enables a high Al content in the β -(Al_xGa_{1-x})₂O₃ barriers. The MOCVD growth has a large temperature window and precise control of the precursor flow, which makes it suitable for growing high-Al-fraction β -(Al_xGa_{1-x})₂O₃ thin films. Such a high Al content is critical to realizing the formation of a 2DEG in the β -(Al_xGa_{1-x})₂O₃/β-Ga₂O₃ heterojunctions and achieving a sufficiently large conduction band offset to confine the electrons [85]. Recent efforts involving the incorporation of Al through MOCVD have achieved 99% incorporation in the (100) orientation. However, the (010) and (−201) orientations exhibited lower Al incorporation, which was limited to 29% and 16%, respectively [89].

Ranga et al. [78] demonstrated n -type degenerate doping in β -(Al_{0.26}Ga_{0.74})₂O₃ thin films grown through MOCVD and employed modulation doping in β -(Al_{0.26}Ga_{0.74})₂O₃/β-Ga₂O₃ heterostructures. The Hall measurements unveiled a high carrier concentration ranging from 0.6 to 7.3 × 10¹⁹ cm⁻³, accompanied by a corresponding electron mobility of 53–27 cm²/V·s within the uniformly doped β -(Al_{0.26}Ga_{0.74})₂O₃ layers. To assess the quality of the Si-doped β -(Al_xGa_{1-x})₂O₃ epilayers, HRXRD measurements were taken to determine the Al composition of these epilayers. The results indicate Al mole fractions of approximately 0.26, closely matching the precursor molar flow ratio (25%) (Figure 7a), indicating that there were no pre-reactions with a complete incorporation of Al. Following the deposition of Ti/Au, Ohmic contact behavior was observed at room temperature. The temperature-dependent carrier concentration and mobility of the epilayers were assessed

using Hall measurements (Figure 7b,c). Among the three samples grown using different silane (SiH_4) flows, it was observed that sample A did not form Ohmic contact below 160 K. All three samples showed degenerate doping, as no carrier freeze-out was evident. To further confirm these observations, Figure 7d shows calculations of the separation from the Fermi level and conduction band considering different Al fraction values (α), where $\alpha = 0.22$ (non-parabolic bands) and $\alpha = 0$ (parabolic bands) for the three samples. This analysis confirmed that sample A exhibited weakly degenerate characteristics, while samples B and C were strongly degenerate. To achieve a total electron sheet charge of $2.3 \times 10^{12} \text{ cm}^{-2}$, modulation doping in a $\beta\text{-(Al}_{0.26}\text{Ga}_{0.74})_2\text{O}_3/\beta\text{-Ga}_2\text{O}_3$ heterostructure was utilized, employing a uniformly doped $\beta\text{-(Al}_{0.26}\text{Ga}_{0.74})_2\text{O}_3$ barrier layer alongside a thin spacer layer, as illustrated in the inset in Figure 7e. In Figure 7e, the HRXRD spectrum of the $\beta\text{-(Al}_{0.26}\text{Ga}_{0.74})_2\text{O}_3/\beta\text{-Ga}_2\text{O}_3$ heterostructures on a Sn-doped substrate is presented. C–V measurements were conducted to measure the charge density and depth relationship. A peak corresponding to the 2DEG was observed near the estimated barrier thickness obtained from HRXRD, indicating modulation doping at this interface. The sudden drop in the C–V profile with depth (Figure 7f) confirms the carrier confinement at the heterointerface. Figure 7g presents the simulated band diagram using a Poisson–Schrödinger solver, which is closely aligned with the measured 2DEG value from the C–V profile.

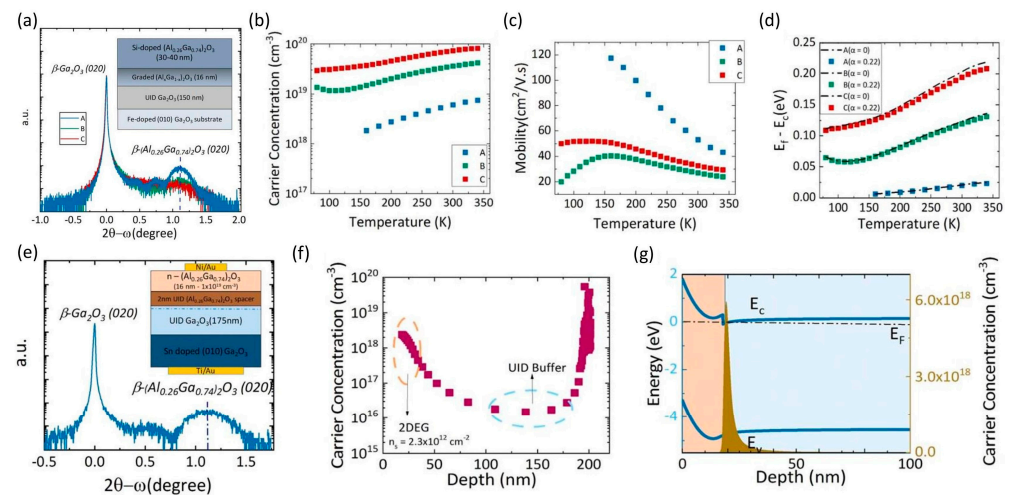


Figure 7. (a) A HRXRD plot of $\beta\text{-(Al}_x\text{Ga}_{1-x})_2\text{O}_3$ epilayers grown using MOCVD (inset: the grown structure). (b) Carrier concentration and (c) mobility vs. temperature plots for three different samples, A, B, and C. (d) Fermi level separation from the conduction band with increasing temperature. (e) A HRXRD plot of $\beta\text{-(Al}_x\text{Ga}_{1-x})_2\text{O}_3$ epilayers grown on Sn-doped substrate (inset: the grown structure). (f) The carrier concentration versus depth profile extracted from C–V measurements. (g) The band diagram simulated from a Poisson–Schrödinger solver. (a–g) reproduced with permission from P. Ranga et al., *Appl. Phys. Express* 12, 111004 (2019) [78]. Copyright 2019 IOP Publishing.

Recently, Wang et al. [90] conducted an extensive study using TCAD simulations to gain insights into $\beta\text{-(Al}_x\text{Ga}_{1-x})_2\text{O}_3/\beta\text{-Ga}_2\text{O}_3$ heterostructures. The impact of the δ -doping concentration, the influence of the δ -doping position, and the effect of the δ -doping width were systematically investigated [90]. Multiple MODFETs have been developed after the successful growth of high-quality $\beta\text{-(Al}_x\text{Ga}_{1-x})_2\text{O}_3/\beta\text{-Ga}_2\text{O}_3$ heterostructures. Ahmadi et al. [91] reported $\beta\text{-(Al}_x\text{Ga}_{1-x})_2\text{O}_3/\beta\text{-Ga}_2\text{O}_3$ MODFETs grown via MBE with Ge as the n -type dopant. Their work resulted in a maximum current density of 20 mA/mm and a pinch-off voltage of -6 V, with a 2DEG sheet charge density of $1.2 \times 10^{13} \text{ cm}^{-2}$. Zhang et al. [86] employed the same structure grown using MBE to fabricate a $\beta\text{-(Al}_x\text{Ga}_{1-x})_2\text{O}_3/\beta\text{-Ga}_2\text{O}_3$ MODFET (Figure 6a). The heterostructure exhibited a high channel mobility at low temperatures, enabling the measurement of the Shubnikov–de Haas (SdH) oscillations in the transverse magnetoresistance under varying magnetic fields per-

pendicular to the sample surface. The calculated 2DEG densities from the SdH oscillations were 1.15×10^{12} and $1.96 \times 10^{12} \text{ cm}^{-2}$ for samples A and B, respectively, aligning with low-field Hall measurements (Figure 6d). The transconductance (g_m) decreased at a higher gate bias due to the reduced modulation efficiency resulting from the charge transfer into the barrier layer. The device exhibited $\sim 10^9$ rectification and an SS of $\sim 91 \text{ mV/Dec}$. The extracted V_{th} was 0.5 V, indicating a normally-off operation. High-frequency small-signal measurements conducted on this device showed a cutoff frequency of 3.1 GHz and a maximum oscillation frequency of 13.1 GHz at a V_{DS} of 10 V and a V_{GS} of 1.5 V. Kalarickal et al. [92] achieved a higher 2DEG sheet charge density, reaching up to $4.7 \times 10^{12} \text{ cm}^{-2}$, along with an effective mobility of $150 \text{ cm}^2/\text{V}\cdot\text{s}$ using an ultra-thin spacer layer of just 1 nm. Increasing the 2DEG density is important as it aids in reducing the R_{on} and boosting the drain current in MODFETs. Moreover, a heightened charge density contributes to better screening of the strong polar optical phonon scattering, ultimately enhancing mobility. With a fixed conduction band offset, reducing the spacer thickness can be used to increase the 2DEG density. Furthermore, given that polar optical phonon scattering already limits mobility ($\sim 200 \text{ cm}^2/\text{V}\cdot\text{s}$), the potential impact of increased remote ionized impurity scattering on the total mobility is expected to be minimal with a 1 nm spacer. To prevent the diffusion of the Si δ -doping through the thin spacer, a lower growth temperature of $610 \text{ }^\circ\text{C}$ was used. Additionally, Kalarickal et al. [93] presented an effective field management approach to $\beta\text{-(Al}_x\text{Ga}_{1-x})_2\text{O}_3/\beta\text{-Ga}_2\text{O}_3$ MODFETs by employing an extremely high-k dielectric, BaTiO₃ ($k > 100$). This innovative strategy facilitated a more uniform electric field distribution within the gate–drain region of the FET. Using this method, average breakdown fields of 1.5 and 4 MV/cm were achieved at gate-to-drain spacings (L_{GD}) of 6 and 0.5 μm , respectively, with a high channel sheet charge density of $1.6 \times 10^{13} \text{ cm}^{-2}$. This resulted in a record PFOM of 376 MW/cm^2 at an L_{GD} of 3 μm .

Zhang et al. [94] demonstrated a double heterostructure MODFET (DHFET), as in Figure 8a. In this configuration, the $\beta\text{-(Al}_x\text{Ga}_{1-x})_2\text{O}_3/\beta\text{-Ga}_2\text{O}_3/\beta\text{-(Al}_x\text{Ga}_{1-x})_2\text{O}_3$ heterostructure acts as a quantum well and provides a 2DEG charge density higher than that of a single heterostructure. The Hall measurements indicated a mobility of $1775 \text{ cm}^2/\text{V}\cdot\text{s}$ at 40 K and $123 \text{ cm}^2/\text{V}\cdot\text{s}$ at room temperature. Figure 8b,c show the output and transfer curves of the demonstrated device with the physical dimensions and the biasing conditions. Figure 8d shows a simulation of the energy band diagram of the double heterostructure with and without parallel conducting channels. The important thing to note is that parallel conducting channels in the $\beta\text{-(Al}_x\text{Ga}_{1-x})_2\text{O}_3$ barrier layers can show up at high-impurity doping levels, as in the upper diagram of Figure 8d. These parasitic channels can lower mobility and affect the device performance. Therefore, precise control of Si doping is necessary to minimize the effect of parasitic conducting channels. The channel mobility at room temperature with the depth profile was extracted from a demonstrated transistor, as in Figure 8e. Later, Kalarickal et al. [95] reported a $\beta\text{-(Al}_{0.18}\text{Ga}_{0.82})_2\text{O}_3/\text{Ga}_2\text{O}_3$ DHFET with an average field of 5.5 MV/cm, where a field management strategy with high-k BaTiO₃ and low-k SiO₂ and Al₂O₃ was also employed. The measured output characteristics of the $\beta\text{-(Al}_{0.18}\text{Ga}_{0.82})_2\text{O}_3/\beta\text{-Ga}_2\text{O}_3$ DHFET showed an R_{on} of $28.6 \text{ }\Omega\cdot\text{mm}$. The corresponding transfer characteristics revealed a rectification ratio of $\sim 10^7$. The device breakdown voltage increased from 0.66 V to 1.11 kV as the L_{GD} was increased from 1.15 to 5.15 μm . Vaidya et al. [96] reported high-performance $\beta\text{-(Al}_x\text{Ga}_{1-x})_2\text{O}_3/\beta\text{-Ga}_2\text{O}_3$ MODFETs with an elevated g_m and a peak current density reaching 74 mA/mm. The small signal frequency measurements revealed impressive cutoff frequencies for the current gain and power gain, measuring 30 and 37 GHz, respectively, at a V_{GS} of 1.2 V and a V_{DS} of 10 V. Joishi et al. [97] demonstrated the breakdown characteristics of a field-plated $\beta\text{-(Al}_{0.22}\text{Ga}_{0.78})_2\text{O}_3/\beta\text{-Ga}_2\text{O}_3$ MODFETs with Si₃N₄ passivation. A high BV of 1.37 kV was shown for a $L_{GD} = 16 \text{ }\mu\text{m}$ device with an $R_{on,sp}$ of $120 \text{ }\Omega\cdot\text{cm}^2$. A comparably high average breakdown field of 3.9 MV/cm was obtained for an $L_{GD} = 320 \text{ nm}$ device. This work shows effective passivation and field management strategies such as gate-connected FPs can significantly enhance the device performance. Recently, Wang et al. [98] explored a novel current aperture vertical tran-

sistor (CAVET) using TCAD simulation by incorporating a $\beta\text{-(Al}_x\text{Ga}_{1-x})_2\text{O}_3/\beta\text{-Ga}_2\text{O}_3$ heterostructure. These results indicate the potential of $\beta\text{-(Al}_x\text{Ga}_{1-x})_2\text{O}_3/\beta\text{-Ga}_2\text{O}_3$ MODFETs.

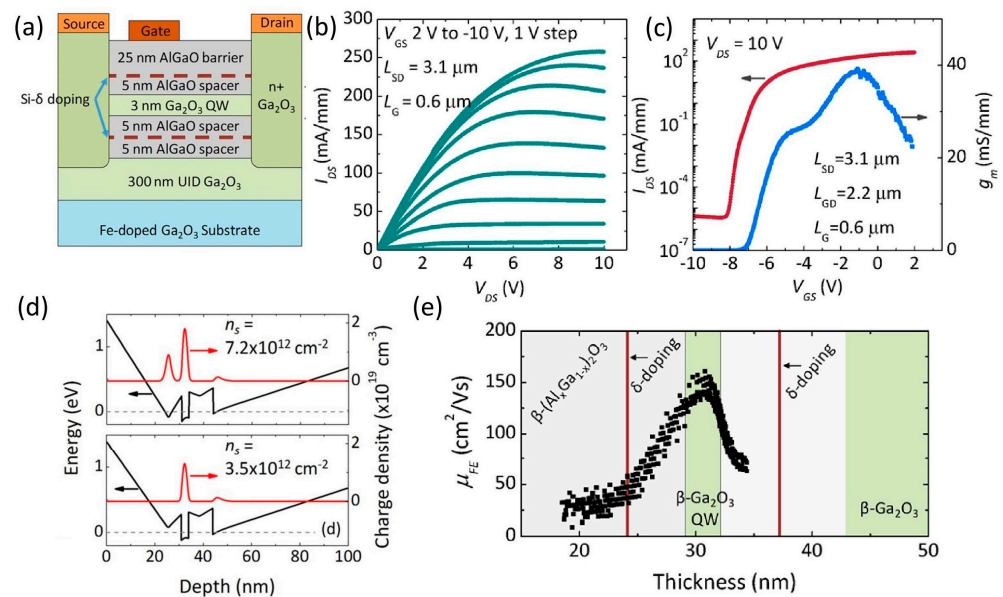


Figure 8. (a) Schematic of a double heterostructure MODFET (DHFET). (b) Output and (c) transfer characteristics of demonstrated device. (d) Energy band diagrams with and without parallel conducting channels and the corresponding 2DEG charge distributions. (e) Depth profile vs. mobility of a demonstrated FET. (a–e) reproduced with permission from Y. Zhang et al., *Appl. Phys. Lett.* 112, 233503 (2018) [94]. Copyright 2018 AIP Publishing.

As the fabrication techniques for $\beta\text{-(Al}_x\text{Ga}_{1-x})_2\text{O}_3/\beta\text{-Ga}_2\text{O}_3$ heterostructures continue to advance, there is a promising future for employing these heterostructures in vertical devices. Nevertheless, the growth of the $\beta\text{-(Al}_x\text{Ga}_{1-x})_2\text{O}_3$ layer is constrained by the relatively slow growth rate, and as the layer thickness increases with a higher Al content, the film quality tends to deteriorate. Consequently, kV-class vertical devices based on $\beta\text{-(Al}_x\text{Ga}_{1-x})_2\text{O}_3/\beta\text{-Ga}_2\text{O}_3$ have not yet been realized. However, the use of UID of $\beta\text{-(Al}_x\text{Ga}_{1-x})_2\text{O}_3$ as a cap layer to enhance the BV of $\beta\text{-Ga}_2\text{O}_3$ SBDs has been explored [99]. Ahmadi et al. [100] investigated $\beta\text{-(Al}_x\text{Ga}_{1-x})_2\text{O}_3/\beta\text{-Ga}_2\text{O}_3$ heterostructures for the fabrication of SBDs with varying Al contents (Figure 9a). The diodes were produced by growing a 400 nm thick $\beta\text{-Ga}_2\text{O}_3$ layer on Sn-doped $\beta\text{-Ga}_2\text{O}_3$ (010) substrates, followed by a 100 nm thick $\beta\text{-(Al}_x\text{Ga}_{1-x})_2\text{O}_3$ layer with four different Al compositions. The HRXRD measurements (Figure 9b) confirmed the different Al compositions to be 0, 0.038, 0.084, and 0.164. The I–V characteristics revealed that similar Schottky barrier heights were observed in the SBDs with varying Al contents, which is attributed to the lateral fluctuations in the alloy composition leading to no variations in the barrier height. Figure 9c shows the temperature-dependent I–V data for an $x = 0.084$ composition. Furthermore, an increase in temperature resulted in a decrease in the ideality factor and an increase in the Schottky barrier height of the devices (Figure 9d), indicating an inhomogeneous Ni-Schottky contact. Sundaram et al. [99] introduced a novel structure to enhance the BV by growing a 30 nm $\beta\text{-(Al}_x\text{Ga}_{1-x})_2\text{O}_3$ capping layer to increase the Schottky barrier height, as shown in Figure 9e. They fabricated and compared $\beta\text{-(Al}_x\text{Ga}_{1-x})_2\text{O}_3$ -capped ($x = 0.22$) SBDs with conventional $\beta\text{-Ga}_2\text{O}_3$ SBDs. Electrical measurements were conducted on both devices to determine the Schottky barrier height, and the resulting I–V curves are presented in Figure 9f. The extracted Schottky barrier heights for the $\beta\text{-Ga}_2\text{O}_3$ -only and $\beta\text{-(Al}_x\text{Ga}_{1-x})_2\text{O}_3$ -capped devices were 1.32 and 1.58 eV, respectively. This indicates an increase of 0.26 eV for the $\beta\text{-(Al}_x\text{Ga}_{1-x})_2\text{O}_3$ -capped sample compared to the $\beta\text{-Ga}_2\text{O}_3$ -only device. In Figure 9g, the reverse I–V characteristics of the two SBDs are shown, where the $\beta\text{-Ga}_2\text{O}_3$ -only device and $\beta\text{-(Al}_x\text{Ga}_{1-x})_2\text{O}_3$ -capped device exhibit BVs of 246 V and 387 V,

respectively. Figure 9h depicts the simulated electric field around the Schottky contact's edge at reverse breakdown. For the β -Ga₂O₃-only device, the maximum electric field under the anode edge was 2.5 MV/cm at breakdown (Figure 9h). In the β -(Al_xGa_{1-x})₂O₃-capped device, the maximum field was 3.6 MV/cm. The additional Schottky barrier height created by the β -(Al_xGa_{1-x})₂O₃ cap at the Schottky interface reduced the thermionic emission (TE) and thermionic field emission (TFE), thereby increasing the device's BV.

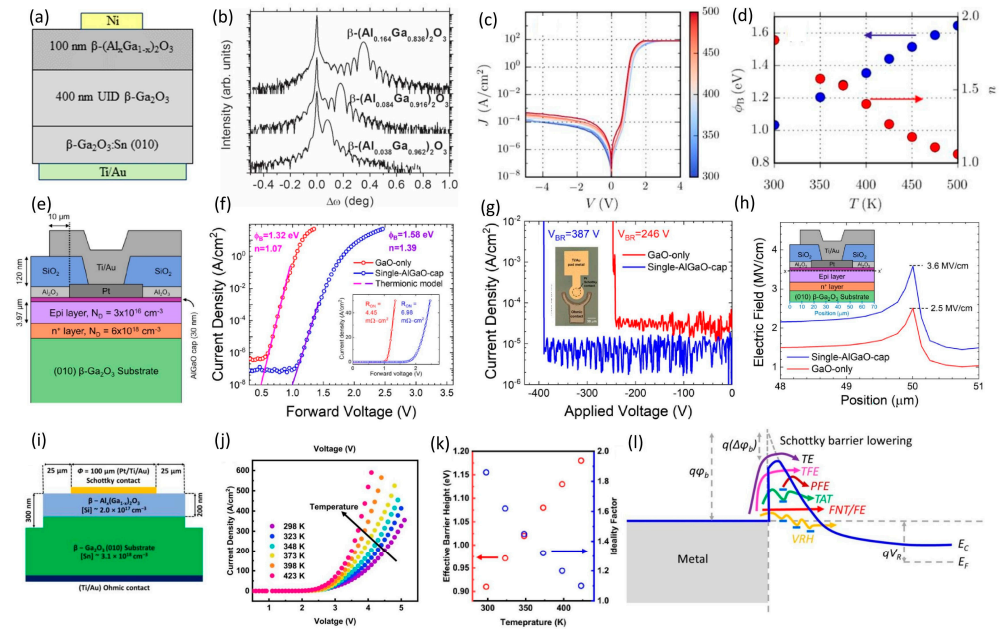


Figure 9. (a) Schematic of vertical β -(Al_xGa_{1-x})₂O₃ SBD. (b) An HRXRD plot of the grown films with different Al compositions of $x = 0, 0.038, 0.084,$ and 0.164 . (c) Temperature-dependent I–V curves for $x = 0.084$ SBD. (d) The variation in Schottky barrier height and ideality factor with temperature as extracted from (c). (e) β -Ga₂O₃ SBD with a thin β -(Al_xGa_{1-x})₂O₃ cap ($x = 0.22$). (f) Forward I–V characteristics on a log scale (inset: forward I–V characteristics on a linear scale). (g) The reverse breakdown of the capped and conventional SBDs. (h) The simulated electric field at the anode edge with and without β -(Al_xGa_{1-x})₂O₃ cap. (i) A fabricated vertical β -(Al_xGa_{1-x})₂O₃ SBD ($x = 0.21$). (j) Temperature-dependent I–V curves. (k) The variation in Schottky barrier height and ideality factor with temperature. (l) Reverse leakage mechanisms of the fabricated SBDs. (a–d) E. Ahmadi et al., *Semicond. Sci. Technol.* 32, 035004 (2017) [100]. Copyright 2017 IOP Publishing. (e–h) reproduced with permission from P. P. Sundaram et al., *J. Vac. Sci. Technol. A* 40, 043211 (2022) [99]. Copyright 2022 American Vacuum Society. (i–l): D.H. Mudiyansele et al., *J. Vac. Sci. Technol. A* 41, 023201 (2023) [101]. Copyright 2023 American Vacuum Society.

To gain a deeper understanding of the leakage mechanisms of β -(Al_xGa_{1-x})₂O₃ SBDs, Mudiyansele et al. [101] conducted a study on the temperature-dependent reverse I–V characteristics of these devices. β -(Al_xGa_{1-x})₂O₃ ($x = 0.21$) thin films were grown via MBE on a (010) Sn-doped β -Ga₂O₃ substrate, as depicted in Figure 9i. An anode made of Pt/Ti/Au was deposited to form the Schottky contact. Figure 9j presents the temperature-dependent forward I–V characteristics of the devices, showing an increasing current density with increasing temperature. Figure 9k displays the Schottky barrier heights and ideality factors of the vertical β -(Al_xGa_{1-x})₂O₃ SBD calculated using the TE theory. As the temperature increased, the barrier height varied from 0.91 to 1.18 eV, while the ideality factor changed from 1.8 to 1.1. These changes are attributed to the non-uniform nature of the metal/semiconductor interface (i.e., inhomogeneous Schottky contact), resulting in the clear temperature-dependent behavior of both parameters. In Figure 9l, the leakage mechanisms for the SBDs are depicted. Different temperature ranges activate distinct processes within the semiconductor, as revealed by the reverse I–V measurements. Because

of the high Schottky barrier height exceeding 1 eV in the vertical $\beta\text{-(Al}_x\text{Ga}_{1-x})_2\text{O}_3$ SBD, the most likely mechanisms include Poole–Frenkel emission (PFE), trap-assisted tunneling (TAT), Fowler–Nordheim tunneling (FNT), field emission (FE), and variable range hopping (VRH). To identify the dominant process, researchers often fit the reverse leakage data using the mathematical expressions of each model. Our analysis identified PFE and TAT as the two dominant mechanisms, with the other mechanisms playing a minor role.

Wan et al. [102] presented a lateral rectifier based on a $\text{NiO}_x/\beta\text{-(Al}_{0.21}\text{Ga}_{0.79})_2\text{O}_3/\beta\text{-Ga}_2\text{O}_3$ heterojunction. The structure of these rectifiers is depicted in Figure 10a, with the $\beta\text{-(Al}_x\text{Ga}_{1-x})_2\text{O}_3/\beta\text{-Ga}_2\text{O}_3$ heterostructure grown using a MOCVD system. NiO_x was deposited using RF magnetron sputtering, and a bilayer structure was employed to optimize the sheet resistance and BV. Figure 10b shows the temperature-dependent forward I–V characteristics and the $R_{on,sp}$ of the devices on a logarithmic scale, while Figure 10c shows the forward I–V characteristics on a linear scale with the extracted turn-on voltage at each temperature. The device current density increased with temperature, while the device turn-on voltage decreased as the temperature increased. Figure 10d shows the reverse I–V characteristics of the devices, where the negative temperature dependence of the BVs was observed, and thus the breakdown mechanism did not involve avalanche breakdown. They further studied devices with different diameters (50, 75, and 100 μm) [103]. The forward I–V curves of the devices with different diameters showed that the inclusion of the alloy did not significantly degrade the turn-on voltage. The highest BV value exceeding 7 kV was achieved in the 75 μm diameter lateral rectifier. A reverse I–V measurement at a low bias (< -100) indicated that the reverse leakage current in this bias range was primarily governed by TFE.

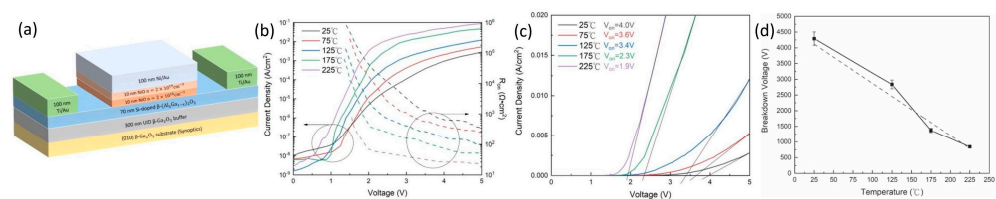


Figure 10. (a) Demonstrated $\text{NiO}_x/\beta\text{-(Al}_{0.21}\text{Ga}_{0.79})_2\text{O}_3/\beta\text{-Ga}_2\text{O}_3$ heterojunction lateral p - n diode. (b) Temperature-dependent forward I–V and $R_{on,sp}$ on a log scale. (c) Temperature-dependent I–V characteristics on a linear scale and extracted turn-on voltages. (d) Variation in BV with temperature. (a–d) reproduced with permission from H.-H. Wan et al., *ECS J. Solid State Sci. Technol.* 12, 075008 (2023) [102]. Copyright 2023 under the terms of CC BY 4.0.

In short, the above research and the development of $\beta\text{-(Al}_x\text{Ga}_{1-x})_2\text{O}_3/\beta\text{-Ga}_2\text{O}_3$ heterostructures have shown considerable promise for power electronics. These heterostructures have been investigated in various device configurations, such as SBDs and MODFETs. The outcomes of these studies provide important insights into their electrical characteristics and potential applications. Further exploration and optimization of these heterostructures may lead to significant advancements in the field.

4. $\beta\text{-Ga}_2\text{O}_3$ Heterojunctions with Other p -Type Materials

In addition to NiO_x , other p -type semiconducting materials with wide bandgaps, such as SiC and GaN, and metal oxides like Cu_2O , CuI, and SnO have shown promise in forming p - n heterojunctions with $\beta\text{-Ga}_2\text{O}_3$. However, the exploration and utilization of these heterojunctions, in contrast to NiO_x , are still in the early stages of development. Montes et al. [104] demonstrated a p - n heterojunction created using mechanically exfoliated $\beta\text{-Ga}_2\text{O}_3$ thermally bonded with p -GaN, as depicted in Figure 11a. The electrical characteristics of the devices are presented in Figure 11b on both the linear and logarithmic scales, while Figure 11c provides a comparison between the p - n diode and a simultaneously fabricated $\beta\text{-Ga}_2\text{O}_3$ SBD. These devices exhibited good temperature behavior, as shown in Figure 11d. Due to a significant number of interface states, the ideality factor for these devices was relatively large and decreased with an increasing temperature.

The turn-on voltage of the devices was approximately 3.6 V at room temperature and decreased to around 2.2 V at 200 °C (Figure 11e). A band diagram of the devices was simulated using Silvaco TCAD in Figure 11f. The ideal turn-on voltage from the simulation was 3.2 V, while most of the fabricated devices exhibited a higher turn-on voltage, mainly due to the mechanical bonding of the p - n heterojunction (Figure 11g). In Figure 11h, an Arrhenius plot showed the conductance as a function of temperature at a forward bias of 3.5 V, demonstrating improved conductivity with increasing temperature. Moreover, p -GaN/ β -Ga₂O₃ diodes were created with varying β -Ga₂O₃ thickness. Figure 11i shows the I–V characteristics of the p - n heterojunction with β -Ga₂O₃ thicknesses of 100 nm and 5 and 20 μ m, indicating similar electrical characteristics across the different thicknesses. Mudiyansele et al. [105] conducted theoretical investigations into edge termination structures for this p - n heterojunction, utilizing a 5 μ m thick β -Ga₂O₃ drift layer, which has enabled the development of kV-class power diodes. Nandi et al. [106] have conducted research on JBS diodes utilizing this heterostructure, examined the switching characteristics of the devices, and obtained information on the reverse recovery behavior. Furthermore, Mudiyansele et al. [107] studied JBS diodes by optimizing the p -GaN regions and varying their shapes to minimize the electric field crowding within the devices. Under forward bias, the Schottky regions became active, while under reverse bias, the p - n junctions effectively reduced the leakage currents. Deep UV photodiodes based on β -Ga₂O₃/SiC heterojunctions were demonstrated [108]. Nakagomi et al. [109] presented a β -Ga₂O₃/SiC heterojunction diode according to the thermal evaporation of Ga in O₂ plasma onto a p -type 6H-SiC substrate. Song et al. [110] investigated a β -Ga₂O₃/4H-SiC MOSFET using fusion bonding.

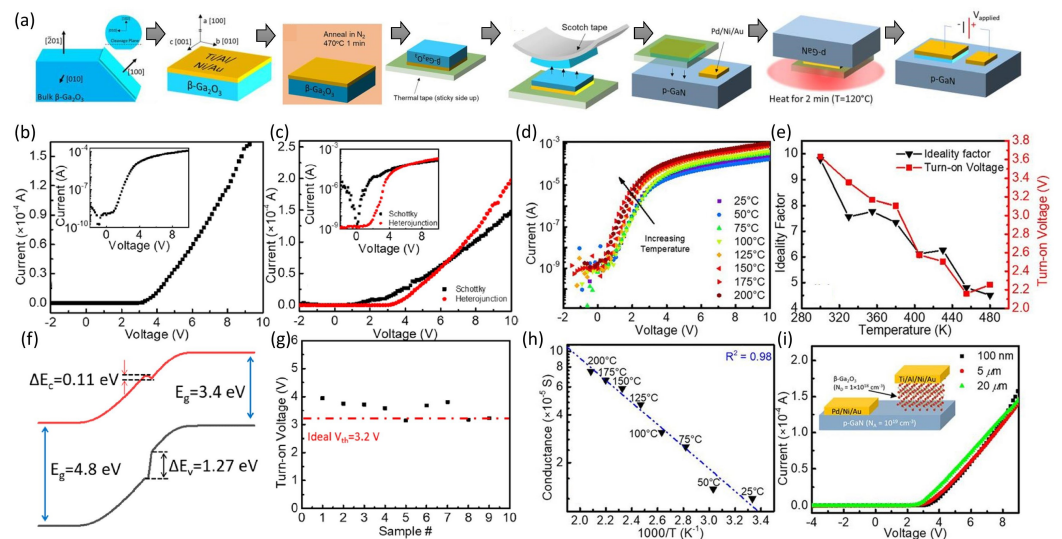


Figure 11. (a) Process of mechanical exfoliation and forming the p -GaN/ β -Ga₂O₃ p - n diodes. (b) The forward I–V curve on a linear scale (inset: forward I–V curve on a log scale). (c) Comparison of forward I–V between the SBD and p - n diode on a linear scale (inset: forward I–V curves on a log scale). (d) Temperature-dependent I–V curves. (e) The variation in ideality factor and turn-on voltage of the device with temperature. (f) Simulated band diagram of the p - n heterojunction. (g) Variation in turn-on voltage in fabricated devices. (h) Arrhenius plot of a device at 3.5 V forward bias. (i) Forward I–V curves for β -Ga₂O₃ with different thicknesses. (a–i) reproduced with permission from J. Montes et al., *Appl. Phys. Lett.* 114, 162103 (2019) [104]. Copyright 2019 AIP Publishing.

Alternative materials such as Cu₂O, CuI, and SnO have also been employed to create p - n heterojunctions with β -Ga₂O₃. Watahiki et al. [111] fabricated p -Cu₂O/ β -Ga₂O₃ diodes, as depicted in Figure 12a. The heterojunction demonstrated a significant forward current, pointing to a low conduction band offset at the p -Cu₂O/ β -Ga₂O₃ interface (Figure 12b). This device exhibited an R_{on} of 8.2 m Ω ·cm² and a BV of 1.49 kV (Figure 12c,d).

An ideality factor of 1.31 suggested the diffusion current as the dominant mechanism. p -CuI/ β -Ga₂O₃ was also demonstrated [112]. Furthermore, Budde et al. [113] reported vertical p -SnO/ β -Ga₂O₃ heterojunction diodes via PAMBE (Figure 12e). The simulated band diagram is depicted in Figure 12f. These diodes exhibited excellent rectification with an ON/OFF ratio of 2×10^8 at ± 1 V, an ideality factor of 1.16, and an $R_{on,sp}$ of $3.9 \text{ m}\Omega \cdot \text{cm}^2$. The temperature-dependent I–V measurements indicated that TE dominated the transport in the forward bias (Figure 12g). The built-in voltage, calculated from the C–V measurements, was 0.96 V, as in Figure 12h. Moreover, Tetzner et al. [114] demonstrated an advanced lateral heterojunction FET (HJFET) utilizing p -type SnO in combination with (100)-oriented n -type β -Ga₂O₃ (Figure 12i). These transistors displayed stable switching properties with ON/OFF current ratios exceeding 10^6 and an $R_{on,sp}$ below $50 \Omega \cdot \text{mm}$, as demonstrated in Figure 12j,k. In the breakdown measurements, a heterojunction transistor with an L_{GD} of $4 \mu\text{m}$ achieved a breakdown voltage of 0.75 kV (Figure 12l) and a calculated BFOM of $178 \text{ MW}/\text{cm}^2$. In summary, p -SnO/ β -Ga₂O₃ and p -Cu₂O/ β -Ga₂O₃ diode structures exhibit relatively lower ideality factors, indicating their potential for high-frequency applications and offer promising performance in terms of R_{on} , BV, and BFOM. However, the calculated critical breakdown field still falls short of the theoretical value for β -Ga₂O₃, possibly due to surface defects during film growth and the absence of electric field management design. Future studies should systematically explore these characteristics as well.

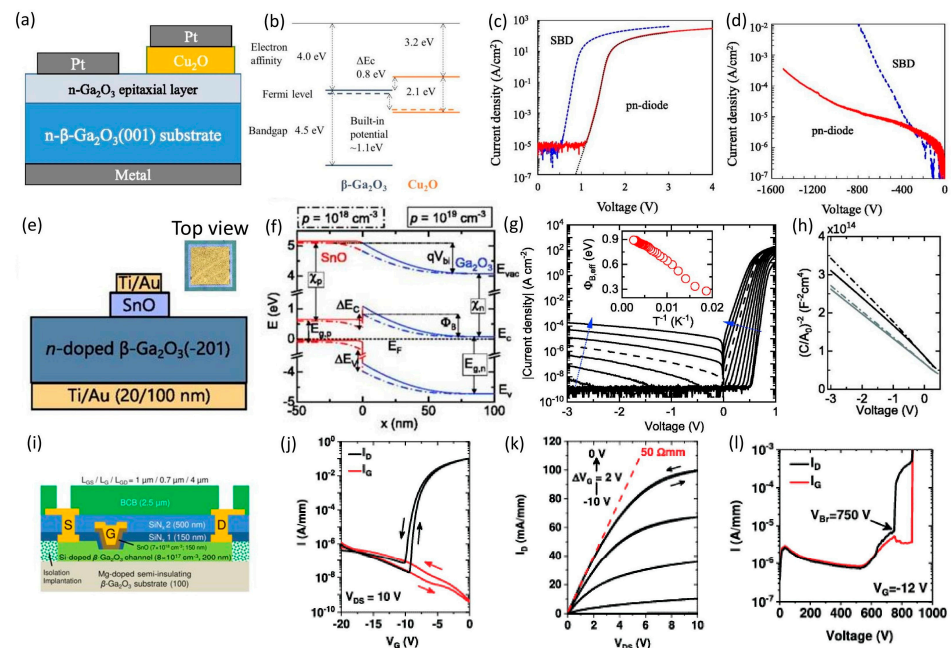


Figure 12. (a) Schematics of Cu₂O/ β -Ga₂O₃ p - n diode and Pt/ β -Ga₂O₃ SBD. (b) Band alignment of Cu₂O/ β -Ga₂O₃ heterojunction. (c) Forward and (d) reverse I–V characteristics of the p - n diode and SBD. (e) Schematic of the vertical SnO/ β -Ga₂O₃ heterojunction diodes. (f) Band diagram of SnO/ β -Ga₂O₃ heterojunction. (g) Temperature-dependent I–V characteristics of SnO/ β -Ga₂O₃ p - n diode on a log scale (inset: variation in barrier height with temperature). (h) $1/C^2$ – V measurements of two p - n diodes. (i) Schematic of SnO/ β -Ga₂O₃ HJFET. (j) Transfer and (k) output characteristics of the fabricated SnO/ β -Ga₂O₃ HJFET with $L_{GD} = 4 \mu\text{m}$. (l) Off-state breakdown of the HJFET. (a–d) reproduced with permission from T. Watahiki et al., *Appl. Phys. Lett.* 111, 222104 (2017) [111]. Copyright 2017 AIP Publishing. (e–h) reproduced with permission from M. Budde et al., *Appl. Phys. Lett.* 117, 252106 (2020) [113]. Copyright 2020 AIP Publishing. (i–l) reproduced with permission from K. Tetzner et al., *Appl. Phys. Lett.* 120, 112110 (2022) [114]. Copyright 2022 AIP Publishing.

These findings highlight the potential to enhance novel materials when combined with β -Ga₂O₃. A key challenge in developing these devices is effectively managing the interface states. The presence of interface states, resulting from factors like the growth or deposition

method and lattice mismatch, can limit the device performance. The introduction of a transition layer, such as h-BN, between these materials could help reduce interface states and lead to an improved device performance.

5. β -Ga₂O₃ Heterostructures with Other UWBG Semiconductors

Researchers are also investigating the use of other UWBG materials such as diamond, AlN, and BN to form heterostructures with β -Ga₂O₃. Diamond is a promising material for next-generation power electronic devices due to its high carrier mobilities (4500 cm²/V·s for electrons and 3800 cm²/V·s for holes), higher critical electric field (>10 MV/cm), higher thermal conductivity (2000 W/m·K), and ultra-wide bandgap (5.5 eV) [115,116]. It also has *p*-type doping with boron (B) and has an acceptor concentration ranging from 10¹⁵ to 10²¹ cm⁻³, which make it an attractive candidate material for exploiting the full potential of β -Ga₂O₃ [117]. Matsumae et al. [118] have demonstrated the direct bonding of β -Ga₂O₃ and diamond substrates. OH-terminated β -Ga₂O₃ and diamond surfaces were directly bonded using a thermal dehydration reaction at low temperatures (250 °C). Recently, MOCVD growth of β -Ga₂O₃ on (001) diamond substrates was demonstrated [119]. Furthermore, heteroepitaxial growth of β -Ga₂O₃ thin films on single crystalline diamond (111) wafers using RF magnetron sputtering was also demonstrated [120]. Mishra et al. [121] conducted a theoretical investigation into the electrical and thermal characteristics of diamond/ β -Ga₂O₃ super-junction Schottky barrier diodes (SJSBDs) with a 20 nm thick Al₂O₃ interlayer. This interlayer will play a crucial role in practical device realization because it protects the Ga₂O₃ from microwave plasma etching during the chemical vapor deposition (CVD) growth of diamond. Furthermore, the oxide interlayer aids in securing the nano-diamond seeds necessary for the growth of polycrystalline diamond (PCD). Additionally, this design permits the attainment of high electric fields in both the *p*-type and *n*-type regions, exploiting the UWBG characteristics of these materials. Achieving a charge balance between the *p* and *n* regions is essential for the device to operate effectively at the highest BV. A charge imbalance would diminish the device performance by inducing an asymmetric electric field within the device, leading to premature breakdown. Notably, the incorporation of a *p*-type diamond into this structure also enhanced the device's thermal performance, addressing one of the main challenges associated with β -Ga₂O₃, i.e., low-thermal conductivity [3], as pointed out earlier. Sittimart et al. [117] employed a low-temperature direct bonding method to fabricate diamond/ β -Ga₂O₃ *p-n* heterojunction diodes (inset Figure 13a). These diodes exhibited an impressive rectifying ratio exceeding 10⁸ at \pm 10 V. Additionally, the leakage current was exceptionally low, measuring less than 10⁻¹² A. The forward I–V curve is presented in Figure 13a. The ideality factor and barrier height for these diodes were estimated to be 2.7 and 1.5 eV, respectively. The band alignment of this heterojunction is illustrated in Figure 13b. In Figure 13c, a comparison is presented between the β -Ga₂O₃ SBD and the diamond/ β -Ga₂O₃ *p-n* heterojunction, highlighting their differences and characteristics. Figure 13d shows the C–V characteristics of one of the demonstrated *p-n* diodes. Malakoutian et al. [122] demonstrated polycrystalline diamond epitaxial growth on β -Ga₂O₃ with a CVD method for device-level thermal management. A thermal conductivity of 110 W/m·K for the diamond and a thermal boundary resistance of 30.2 m²K/GW were measured. Recently, Rahaman et al. [123] demonstrated the mechanical integration of diamond/ β -Ga₂O₃ as an effortless fabrication method to demonstrate a *p-n* heterojunction, as in Figure 13e. The devices show a remarkable ON/OFF ratio of 10⁸ and a low ideality factor of 1.28, while the device operation spans from 25 °C up to 125 °C (Figure 13f,g). This work provides a novel pathway for integrating UWBG material with different thermal expansion coefficients.

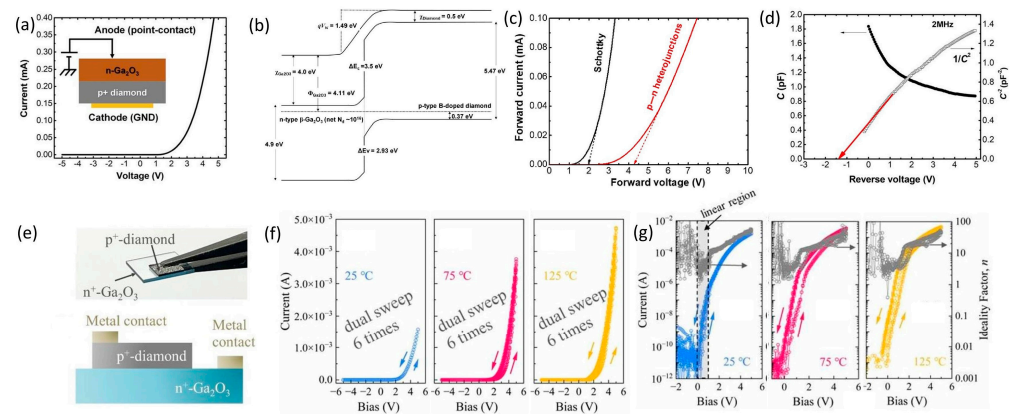


Figure 13. (a) Forward I–V characteristics of a diamond/ β -Ga₂O₃ p - n diode (inset: demonstrated p - n diode with thermal bonding). (b) The simulated band diagram. (c) Forward I–V of characteristics a SBD and a p - n diode. (d) C–V measurements of a p - n diode. (e) Mechanically integrated diamond/ β -Ga₂O₃ p - n diode. (f) Temperature-dependent forward I–V curves on a linear scale. (g) Temperature-dependent forward I–V curve and the ideality factor on a log scale. (a–d) reproduced with permission from P. Sittimart et al., *AIP. Adv.* 11, 105114 (2021) [117]. Copyright 2021 under the terms of CC BY 4.0. (e–g) reproduced from I. Rahaman et al., arXiv:2311.16323 (2023) [123].

AlN exhibits a wide bandgap of 6.2 eV, making it highly suitable for power applications [124]. Chen et al. [125] conducted a study on the band alignment of AlN/ β -Ga₂O₃ heterostructures and determined valence band offsets of 0.09 eV (type II alignment) for AlN grown via plasma-enhanced atomic layer deposition (PEALD) on β -Ga₂O₃ and 0.72 eV (type I alignment) for AlN prepared using thermal atomic layer deposition (T-ALD) on β -Ga₂O₃. Song et al. [126] explored an AlN/ β -Ga₂O₃ heterostructure, employing polarization-induced doping to create high-performance enhancement-mode transistors with a 2DEG concentration reaching up to $8.1 \times 10^{19} \text{ cm}^{-3}$ (Figure 14a). A p -GaN gate was utilized to achieve a normally-off operation with a positive V_{th} . In Figure 14b, the distribution of the polarization charge in the different material regions is depicted, and Figure 14c shows the band diagram and 2DEG confinement, with Figure 14d displaying the device's output characteristics. Nonetheless, growing high-quality AlN or Al-rich AlGaN thin films on β -Ga₂O₃ with good interfaces remains a challenge. Furthermore, since GaN has a narrower bandgap compared to β -Ga₂O₃, p -GaN itself has a lower critical field, which could potentially impact the device breakdown performance. Alternatively, using wider-bandgap p -type materials like p -AlGaN layers may offer advantages for gate materials. Furthermore, researchers are actively exploring the use of UWBG materials such as AlN and h-BN thin interlayers for β -Ga₂O₃ SBDs to achieve higher Schottky barrier heights and BVs. Recently, Baskaran et al. [127] investigated an AlN/ β -Ga₂O₃ high-electron-mobility transistor (HEMT) on a SiC substrate for power converters and RF applications. Similar to AlN, BN is emerging as a UWBG material with a bandgap of ~ 6.0 eV and a critical field of ~ 10 MV/cm [128–130]. However, BN predominantly functions as a dielectric material rather than a semiconductor. A recent study by Xu et al. [130] showcased a kV-class β -Ga₂O₃ metal–insulator–semiconductor (MIS) diode incorporating a thin BN nitride layer aimed at enhancing device breakdown. The introduction of a 2.8 nm thin BN layer (Figure 14e) significantly elevated the device breakdown from 0.73 to 1.03 kV, highlighting the potential of this approach (Figure 14h). It is worth noting that this enhancement may result in an increased turn-on voltage and $R_{on,sp}$ in the devices. Nevertheless, this technique serves as an effective means of tuning the device breakdown voltage. Figure 14f,g depict the forward I–V curves of both diodes, with and without the BN interlayer, on the linear and log scales. These results indicate that the combination of UWBG materials with Ga₂O₃ opens up new device architectures to explore.

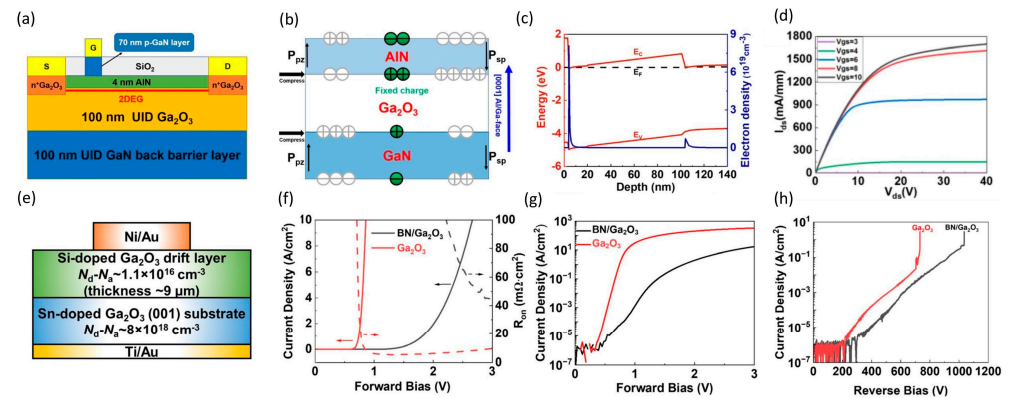


Figure 14. (a) AlN/ β -Ga₂O₃ heterostructure FET. (b) The variation in polarization charges across different materials. (c) Simulated band diagram. (d) The output characteristics of the device. (e) BN/ β -Ga₂O₃ MIS diode. The forward I–V curve of conventional SBD and MIS diode on (f) a linear scale and (g) a log scale. (h) Reverse breakdown of both diodes. (a–d) reproduced with permission from K. Song et al., *J. Phys. D: Appl. Phys.* 53, 345107 (2020) [126]. Copyright 2020 IOP Publishing. (e–h) reproduced with permission from M. Xu et al., *Appl. Phys. Lett.* 123, 232107 (2023) [130]. Copyright 2023 AIP Publishing.

6. β -Ga₂O₃ Heterostructures with 2D Materials

Recent years have witnessed significant advancements in 2D materials such as MoS₂, WS₂, WSe₂, BP, and graphene [131,132]. Researchers have also explored the integration of 2D materials with β -Ga₂O₃. This section discusses some of the noteworthy research efforts and the latest developments. Yan et al. [133] demonstrated graphene/ β -Ga₂O₃ vertical barristor heterostructures, and the device structure is depicted in Figure 15a. The fabrication process began with the mechanical exfoliation and transfer of graphene onto a SiO₂/Si wafer, with the SiO₂ layer measuring 285 nm in thickness. Next, β -Ga₂O₃ was exfoliated and transferred onto the wafer, where it overlapped with the graphene flake. β -Ga₂O₃ was intentionally kept undoped to provide a reasonable estimate of the breakdown field. After that, the contact regions were defined using e-beam lithography, followed by Ti/Au (5/45 nm) metal evaporation. Figure 15b presents a cross-sectional energy band diagram of the heterostructure, illustrating the charge transport mechanisms under different biasing conditions. The graphene layer plays a crucial role in enabling electron injection while enabling a high electric field due to the back-gate (Si substrate) bias. Cross-sectional HRTEM images of the fabricated graphene/ β -Ga₂O₃ heterostructure are showcased in Figure 15c. Electrical measurements revealed a remarkable breakdown field of 5.2 MV/cm perpendicular to the (100) plane.

Kim et al. [134] demonstrated a depletion-mode β -Ga₂O₃ HJFET with an *n*-channel configuration, achieved via van der Waals bonding to an exfoliated *p*-WSe₂ flake, as shown in Figure 15d. The use of van der Waals interaction allows for layered materials separated from their bulk crystals to be assembled into a strain-free heterostructure. Figure 15e shows a band diagram of the device with its conduction and valence band offsets. The *p*-WSe₂/ β -Ga₂O₃ heterostructure diode exhibited typical diode characteristics with a rectifying ratio of $\sim 10^5$. The layered HJFETs displayed exceptional output (Figure 15f) and transfer characteristics. These devices boasted a high ON/OFF ratio of $\sim 10^8$ and a low SS of ~ 133 mV/Dec. Saturated output currents were observed with a V_{th} of -5.1 V, and a three-terminal breakdown voltage of 144 V was obtained. Leblanc et al. [135] demonstrated *p*-*n* heterojunctions using *p*-WSe₂, WS₂, and BP on β -Ga₂O₃, and the fabricated device structure is depicted in Figure 15g. Their study focused on optimizing 2D/3D vertical diodes on β -Ga₂O₃ by considering three key factors, including the β -Ga₂O₃ crystal orientation, the choice of 2D material, and the type of metal contact. The I–V characteristics of the *p*-*n* diodes in (-201) β -Ga₂O₃ orientations are presented in Figure 15h. Figure 15i shows the variation in the ideality factor with the choice of 2D material and β -Ga₂O₃

crystal orientations. These results suggest that 2D/3D β -Ga₂O₃ vertical heterojunctions can be optimized by employing substrate orientation (-201), combining it with 2D WS₂ exfoliated layers and Ti contact. These optimized devices exhibited record rectification ratios ($>10^6$) while maintaining a high ON-current density ($>10^3$ Acm⁻²), making them promising for applications in power rectifiers. The above results showcase the potential of 2D material/ β -Ga₂O₃ for transistors and diodes.

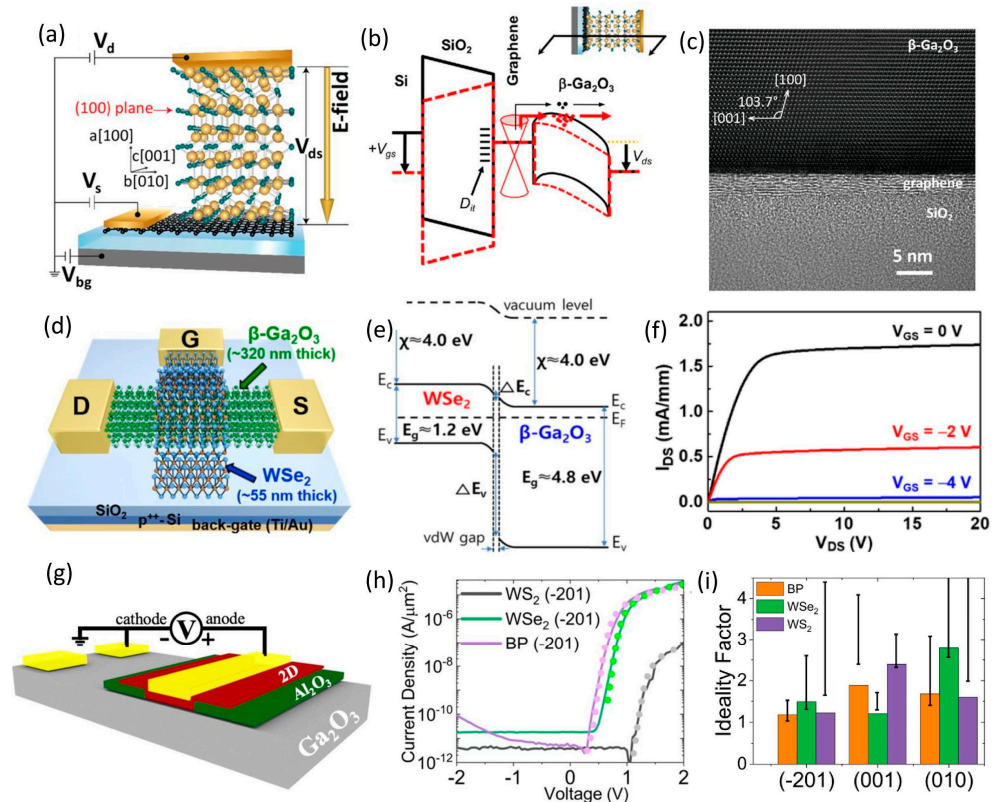


Figure 15. (a) Demonstrated graphene/ β -Ga₂O₃ heterostructure. (b) The simulated band diagram of SiO₂/graphene/ β -Ga₂O₃. (c) HRTEM image of the structure. (d) Schematics of WSe₂/ β -Ga₂O₃ HJFET. (e) The band diagram of WSe₂/ β -Ga₂O₃ heterojunction. (f) Output characters of the WSe₂/ β -Ga₂O₃ HJFET. (g) Schematic of 2D/3D β -Ga₂O₃ p - n diode structure. (h) Forward I–V curves on (-201) plane with WS₂, WSe₂, and BP 2D materials. (i) The variation in ideality factor with different 2D materials and β -Ga₂O₃ planar orientation. (a–c) reproduced with permission from X. Yan et al., *Appl. Phys. Lett.* 112, 032101 (2018) [133]. Copyright 2018 AIP Publishing. (d–f) reproduced with permission from J. Kim et al., *ACS Appl. Mater. Interfaces* 10, 29724 (2018) [134]. Copyright 2018 American Chemical Society. (g–i) reproduced with permission from C. Leblanc et al., *Nanoscale* 15, 9964 (2023) [135]. Copyright 2023 RSC Publishing.

7. Conclusions and Outlook

β -Ga₂O₃ heterostructures and heterojunctions hold significant promise for future power electronics technology advancements. A wide range of heterojunctions/heterostructures and configurations have been explored to harness the unique properties of β -Ga₂O₃ for high-power electronics. NiO_x/ β -Ga₂O₃ heterojunctions open the door for advanced power devices, high-frequency applications, and enhanced functionality. Further optimizations and innovations in incorporating NiO_x/ β -Ga₂O₃ heterostructures into power devices can be expected, and the stability and reliability of such devices warrant special attention. Precise control over the p -type doping of NiO_x is essential to achieve the necessary charge balance between the p - and n -type regions, as any imbalance can hinder the device BV and overall performance. While researchers have demonstrated some degree of tunability in p -type doping, further optimization of NiO_x/ β -Ga₂O₃ heterojunction diodes is warranted.

Exploring various edge termination structures and multidimensional device architectures is crucial to surpass unipolar BFOM limitations. Novel device architectures hold promise for achieving higher performance levels. β -(Al_xGa_{1-x})₂O₃/ β -Ga₂O₃ heterostructures have unique properties, such as high breakdown voltages and excellent 2DEG control, making them the workhorse for high-frequency devices. In these heterostructures, precise control over the Si δ -doping channel width and position is paramount. At elevated doping levels, parasitic conduction channels may arise, emphasizing the importance of accurate Si doping for an optimal device performance. Implementing multiple-channel devices with multiple quantum wells could enhance the device performance compared to single- or double-channel devices. The inclusion of UWBG materials like diamond, AlN, and BN brings new opportunities for β -Ga₂O₃ electronics as both device active regions and passivation structures. The growth of wide- and ultra-wide-bandgap materials on Ga₂O₃ necessitates reducing the defect density and improving the material quality due to significant lattice mismatches. Interface engineering and optimized growth techniques hold the potential to enhance the material quality and consequently the device performance. Furthermore, the versatile nature of β -Ga₂O₃ allows it to be combined with different materials, including 2D materials like graphene, MoS₂, WS₂, WSe₂, and BP for novel device applications, and new and exciting material combinations are expected. Incorporating 2D materials presents challenges, as the surface roughness plays a crucial role in promoting the adhesion between Ga₂O₃ and 2D materials. Future developments may involve exploring new material combinations and device configurations that leverage the anisotropic nature of β -Ga₂O₃. Additionally, improving the Ohmic and Schottky contacts in 2D/3D β -Ga₂O₃ devices is essential to enhancing their current transport capabilities. While there are challenges, such as interface engineering and material compatibility, active research is ongoing to address these issues. Furthermore, issues arising from the low thermal conductivity of Ga₂O₃ can be mitigated with the use of heterostructures involving integration with high-thermal-conductivity diamond and SiC. The research on β -Ga₂O₃ heterostructures and heterojunctions has the potential to significantly expand the capability of Ga₂O₃ power electronics and facilitate their maturity. This review can be a valuable reference for recent developments in Ga₂O₃-based heterojunctions and serve as an important gateway to further development of Ga₂O₃-based electronics and their heterostructures to address future energy demands.

Author Contributions: Conceptualization, D.H.M. and H.F.; writing—original draft preparation, D.H.M., B.D., J.A., D.W., Z.H. and H.F.; writing—review and editing, D.H.M., B.D., K.F., Y.Z. and H.F.; supervision, K.F., Y.Z. and H.F.; funding acquisition, H.F. All authors have read and agreed to the published version of the manuscript.

Funding: This work was supported as part of ULTRA, an Energy Frontier Research Center funded by the U.S. Department of Energy (DOE), the Office of Science, Basic Energy Sciences (BES), under Award # DE-SC0021230. This work is also partially supported by the National Science Foundation (NSF) under Award # 2302696.

Data Availability Statement: The data supporting the results and conclusions of this study are available within the article.

Conflicts of Interest: The authors declare no conflicts of interest.

References

1. *Gallium Oxide*; Springer: Berlin/Heidelberg, Germany, 2020; Volume 293. [CrossRef]
2. Higashiwaki, M.; Sasaki, K.; Kuramata, A.; Masui, T.; Yamakoshi, S. Gallium Oxide (Ga₂O₃) Metal-Semiconductor Field-Effect Transistors on Single-Crystal β -Ga₂O₃ (010) Substrates. *Appl. Phys. Lett.* **2012**, *100*, 013504. [CrossRef]
3. Higashiwaki, M. β -Ga₂O₃ Material Properties, Growth Technologies, and Devices: A Review. *AAPPS Bull.* **2022**, *32*, 3. [CrossRef]
4. Tolbert, L.M. *Power Electronics for Distributed Energy Systems and Transmission and Distribution Applications: Assessing the Technical Needs for Utility Applications*; Oak Ridge National Laboratory: Oak Ridge, TN, USA, 2005.
5. Wang, C.; Zhang, J.; Xu, S.; Zhang, C.; Feng, Q.; Zhang, Y.; Ning, J.; Zhao, S.; Zhou, H.; Hao, Y. Progress in state-of-the-art technologies of Ga₂O₃ devices. *J. Phys. D Appl. Phys.* **2021**, *54*, 243001. [CrossRef]

6. Green, A.J.; Speck, J.; Xing, G.; Moens, P.; Allerstam, F.; Gumaelius, K.; Neyer, T.; Arias-Purdue, A.; Mehrotra, V.; Kuramata, A.; et al. β -Gallium Oxide Power Electronics. *APL Mater.* **2022**, *10*, 029201. [[CrossRef](#)]
7. Chabak, K.D.; Leedy, K.D.; Green, A.J.; Mou, S.; Neal, A.T.; Asel, T.; Heller, E.R.; Hendricks, N.S.; Liddy, K.; Crespo, A.; et al. Lateral β -Ga₂O₃ Field Effect Transistors. *Semicond. Sci. Technol.* **2020**, *35*, 013002. [[CrossRef](#)]
8. Pearton, S.J.; Yang, J.; Cary, P.H., IV; Ren, F.; Kim, J.; Tadjer, M.J.; Mastro, M.A. A Review of Ga₂O₃ Materials, Processing, and Devices. *Appl. Phys. Rev.* **2018**, *5*, 011301. [[CrossRef](#)]
9. Mastro, M.A.; Eddy, C.R., Jr.; Tadjer, M.J.; Hite, J.K.; Kim, J.; Pearton, S.J. Assessment of the (010) β -Ga₂O₃ Surface and Substrate Specification. *J. Vac. Sci. Technol. A* **2020**, *39*, 013408. [[CrossRef](#)]
10. Goto, K.; Konishi, K.; Murakami, H.; Kumagai, Y.; Monemar, B.; Higashiwaki, M.; Kuramata, A.; Yamakoshi, S. Halide Vapor Phase Epitaxy of Si Doped β -Ga₂O₃ and Its Electrical Properties. *Thin Solid Films* **2018**, *666*, 182–184. [[CrossRef](#)]
11. Higashiwaki, M. MBE Growth and Device Applications of Ga₂O₃. In *Molecular Beam Epitaxy*; John Wiley & Sons, Inc.: Hoboken, NJ, USA, 2019; pp. 411–422. ISBN 9781119354987.
12. Seryogin, G.; Alema, F.; Valente, N.; Fu, H.; Steinbrunner, E.; Neal, A.T.; Mou, S.; Fine, A.; Osinsky, A. MOCVD Growth of High Purity Ga₂O₃ Epitaxial Films Using Trimethylgallium Precursor. *Appl. Phys. Lett.* **2020**, *117*, 262101. [[CrossRef](#)]
13. Sinha, G.; Adhikary, K.; Chaudhuri, S. Effect of Annealing Temperature on Structural Transformation of Gallium Based Nanocrystalline Oxide Thin Films and Their Optical Properties. *Opt. Mater.* **2007**, *29*, 718–722. [[CrossRef](#)]
14. Suman, S.; Mukurala, N.; Kushwaha, A.K. Annealing Induced Surface Restructuring in Hydrothermally Synthesized Gallium Oxide Nano-Cuboids. *J. Cryst. Growth* **2021**, *554*, 125946. [[CrossRef](#)]
15. Fujihara, S.; Shibata, Y.; Hosono, E. Chemical Deposition of Rodlike GaOOH and β -Ga₂O₃ Films Using Simple Aqueous Solutions. *J. Electrochem. Soc.* **2005**, *152*, C764. [[CrossRef](#)]
16. Ghazali, N.M.; Mahmood, M.R.; Yasui, K.; Hashim, A.M. Electrochemically Deposited Gallium Oxide Nanostructures on Silicon Substrates. *Nanoscale Res. Lett.* **2014**, *9*, 120. [[CrossRef](#)]
17. Chiang, J.-L.; Yadlapalli, B.K.; Chen, M.-I.; Wu, D.-S. A Review on Gallium Oxide Materials from Solution Processes. *Nanomaterials* **2022**, *12*, 3601. [[CrossRef](#)]
18. Al-Hardan, N.H.; Abdul Hamid, M.A.; Jalar, A.; Firdaus-Raih, M. Unleashing the Potential of Gallium Oxide: A Paradigm Shift in Optoelectronic Applications for Image Sensing and Neuromorphic Computing Applications. *Mater. Today Phys.* **2023**, *38*, 101279. [[CrossRef](#)]
19. Asif, M.; Kumar, A. Resistive Switching in Emerging Materials and Their Characteristics for Neuromorphic Computing. *Mater. Today Electron* **2022**, *1*, 100004. [[CrossRef](#)]
20. Neal, A.T.; Mou, S.; Rafique, S.; Zhao, H.; Ahmadi, E.; Speck, J.S.; Stevens, K.T.; Blevins, J.D.; Thomson, D.B.; Moser, N.; et al. Donors and Deep Acceptors in β -Ga₂O₃. *Appl. Phys. Lett.* **2018**, *113*, 062101. [[CrossRef](#)]
21. Ma, N.; Tanen, N.; Verma, A.; Guo, Z.; Luo, T.; Xing, H.; Jena, D. Intrinsic Electron Mobility Limits in β -Ga₂O₃. *Appl. Phys. Lett.* **2016**, *109*, 212101. [[CrossRef](#)]
22. Kang, Y.; Krishnaswamy, K.; Peelaers, H.; Van de Walle, C.G. Fundamental Limits on the Electron Mobility of β -Ga₂O₃. *J. Phys. Condens. Matter* **2017**, *29*, 234001. [[CrossRef](#)]
23. Ghosh, K.; Singiseti, U. Ab Initio Calculation of Electron–Phonon Coupling in Monoclinic β -Ga₂O₃ Crystal. *Appl. Phys. Lett.* **2016**, *109*, 072102. [[CrossRef](#)]
24. Ghosh, K.; Singiseti, U. Ab Initio Velocity-Field Curves in Monoclinic β -Ga₂O₃. *J. Appl. Phys.* **2017**, *122*, 035702. [[CrossRef](#)]
25. Guo, Z.; Verma, A.; Wu, X.; Sun, F.; Hickman, A.; Masui, T.; Kuramata, A.; Higashiwaki, M.; Jena, D.; Luo, T. Anisotropic Thermal Conductivity in Single Crystal β -Gallium Oxide. *Appl. Phys. Lett.* **2015**, *106*, 111909. [[CrossRef](#)]
26. Gopalan, P.; Knight, S.; Chanana, A.; Stokey, M.; Ranga, P.; Scarpulla, M.A.; Krishnamoorthy, S.; Darakchieva, V.; Galazka, Z.; Irmscher, K.; et al. The Anisotropic Quasi-Static Permittivity of Single-Crystal β -Ga₂O₃ Measured by Terahertz Spectroscopy. *Appl. Phys. Lett.* **2020**, *117*, 252103. [[CrossRef](#)]
27. Fu, H.; Chen, H.; Huang, X.; Baranowski, I.; Montes, J.; Yang, T.-H.; Zhao, Y. A Comparative Study on the Electrical Properties of Vertical (201) and (010) β -Ga₂O₃ Schottky Barrier Diodes on EFG Single-Crystal Substrates. *IEEE Trans. Electron Devices* **2018**, *65*, 3507–3513. [[CrossRef](#)]
28. Lyons, J.L. A Survey of Acceptor Dopants for β -Ga₂O₃. *Semicond. Sci. Technol.* **2018**, *33*, 05LT02. [[CrossRef](#)]
29. He, H.; Orlando, R.; Blanco, M.A.; Pandey, R.; Amzallag, E.; Baraille, I.; Rérat, M. First-Principles Study of the Structural, Electronic, and Optical Properties of Ga₂O₃ in Its Monoclinic and Hexagonal Phases. *Phys. Rev. B* **2006**, *74*, 195123. [[CrossRef](#)]
30. Gake, T.; Kumagai, Y.; Oba, F. First-Principles Study of Self-Trapped Holes and Acceptor Impurities in Ga₂O₃ Polymorphs. *Phys. Rev. Mater.* **2019**, *3*, 44603. [[CrossRef](#)]
31. Ji, X.; Lu, C.; Yan, Z.; Shan, L.; Yan, X.; Wang, J.; Yue, J.; Qi, X.; Liu, Z.; Tang, W.; et al. A Review of Gallium Oxide-Based Power Schottky Barrier Diodes. *J. Phys. D Appl. Phys.* **2022**, *55*, 443002. [[CrossRef](#)]
32. Higashiwaki, M.; Wong, M.H.; Goto, K.; Murakami, H.; Kumagai, Y. (Keynote) Nitrogen-Ion Implantation Doping of Ga₂O₃ and Its Application to Transistors. *ECS Meet. Abstr.* **2019**, MA2019-02, 1169. [[CrossRef](#)]
33. Zhang, L.; Yan, J.; Zhang, Y.; Li, T.; Ding, X. A Comparison of Electronic Structure and Optical Properties between N-Doped β -Ga₂O₃ and N–Zn Co-Doped β -Ga₂O₃. *Phys. B Condens. Matter* **2012**, *407*, 1227–1231. [[CrossRef](#)]
34. Shivani; Kaur, D.; Ghosh, A.; Kumar, M. A Strategic Review on Gallium Oxide Based Power Electronics: Recent Progress and Future Prospects. *Mater. Today Commun.* **2022**, *33*, 104244. [[CrossRef](#)]

35. Lu, X.; Deng, Y.; Pei, Y.; Chen, Z.; Wang, G. Recent Advances in NiO/Ga₂O₃ Heterojunctions for Power Electronics. *J. Semicond.* **2023**, *44*, 061802. [[CrossRef](#)]
36. Kaplar, R.J.; Allerman, A.A.; Armstrong, A.M.; Crawford, M.H.; Dickerson, J.R.; Fischer, A.J.; Baca, A.G.; Douglas, E.A. Review—Ultra-Wide-Bandgap AlGa_N Power Electronic Devices. *ECS J. Solid State Sci. Technol.* **2017**, *6*, Q3061. [[CrossRef](#)]
37. Tsao, J.Y.; Chowdhury, S.; Hollis, M.A.; Jena, D.; Johnson, N.M.; Jones, K.A.; Kaplar, R.J.; Rajan, S.; Van de Walle, C.G.; Bellotti, E.; et al. Ultrawide-Bandgap Semiconductors: Research Opportunities and Challenges. *Adv. Electron Mater.* **2018**, *4*, 1600501. [[CrossRef](#)]
38. Di Girolamo, D.; Di Giacomo, F.; Matteocci, F.; Marrani, A.G.; Dini, D.; Abate, A. Progress, Highlights and Perspectives on NiO in Perovskite Photovoltaics. *Chem. Sci.* **2020**, *11*, 7746–7759. [[CrossRef](#)]
39. Zhang, B.; Su, J.; Guo, X.; Zhou, L.; Lin, Z.; Feng, L.; Zhang, J.; Chang, J.; Hao, Y. NiO/Perovskite Heterojunction Contact Engineering for Highly Efficient and Stable Perovskite Solar Cells. *Adv. Sci.* **2020**, *7*, 1903044. [[CrossRef](#)] [[PubMed](#)]
40. Kokubun, Y.; Kubo, S.; Nakagomi, S. All-Oxide p–n Heterojunction Diodes Comprising p-Type NiO and n-Type β-Ga₂O₃. *Appl. Phys. Express* **2016**, *9*, 091101. [[CrossRef](#)]
41. Li, J.-S.; Xia, X.; Chiang, C.-C.; Hays, D.C.; Gila, B.P.; Craciun, V.; Ren, F.; Pearton, S.J. Deposition of Sputtered NiO as a P-Type Layer for Heterojunction Diodes with Ga₂O₃. *J. Vac. Sci. Technol. A* **2022**, *41*, 013405. [[CrossRef](#)]
42. Schlupp, P.; Splith, D.; von Wenckstern, H.; Grundmann, M. Electrical Properties of Vertical P-NiO/n-Ga₂O₃ and p-ZnCo₂O₄/n-Ga₂O₃ Pn-Heterodiode Ga₂O₃es. *Phys. Status Solidi (a)* **2019**, *216*, 1800729. [[CrossRef](#)]
43. Mudiyansele, D.H.; Mandia, R.; Wang, D.; Adivarahan, J.; He, Z.; Fu, K.; Zhao, Y.; McCartney, M.R.; Smith, D.J.; Fu, H. Anisotropic Electrical Properties of NiOx/β-Ga₂O₃p-n Heterojunctions on (201), (001), and (010) Crystal Orientations. *Appl. Phys. Express* **2023**, *16*, 094002. [[CrossRef](#)]
44. Hajakbari, F. Characterization of Nanocrystalline Nickel Oxide Thin Films Prepared at Different Thermal Oxidation Temperatures. *J. Nanostruct. Chem.* **2020**, *10*, 97–103. [[CrossRef](#)]
45. Xia, X.; Li, J.-S.; Chiang, C.-C.; Yoo, T.J.; Ren, F.; Kim, H.; Pearton, S.J. Annealing Temperature Dependence of Band Alignment of NiO/β-Ga₂O₃. *J. Phys. D Appl. Phys.* **2022**, *55*, 385105. [[CrossRef](#)]
46. Ma, Y.; Qin, Y.; Porter, M.; Spencer, J.; Du, Z.; Xiao, M.; Wang, B.; Wang, Y.; Jacobs, A.G.; Wang, H.; et al. Wide-Bandgap Nickel Oxide with Tunable Acceptor Concentration for Multidimensional Power Devices. *Adv. Electron Mater.* **2023**, 2300662. [[CrossRef](#)]
47. Li, J.-S.; Chiang, C.-C.; Xia, X.; Yoo, T.J.; Ren, F.; Kim, H.; Pearton, S.J. Demonstration of 4.7 KV Breakdown Voltage in NiO/β-Ga₂O₃ Vertical Rectifiers. *Appl. Phys. Lett.* **2022**, *121*, 042105. [[CrossRef](#)]
48. Attri, R.; Panda, D.P.; Ghatak, J.; Rao, C.N.R. High Crystalline Epitaxial Thin Films of NiO by Plasma-Enhanced ALD and Their Properties. *APL Mater.* **2023**, *11*, 091105. [[CrossRef](#)]
49. Liao, C.; Lu, X.; Xu, T.; Fang, P.; Deng, Y.; Luo, H.; Wu, Z.; Chen, Z.; Liang, J.; Pei, Y.; et al. Optimization of NiO/β-Ga₂O₃ Heterojunction Diodes for High-Power Application. *IEEE Trans. Electron Devices* **2022**, *69*, 5722–5727. [[CrossRef](#)]
50. Wrobel, F.; Park, H.; Sohn, C.; Hsiao, H.-W.; Zuo, J.-M.; Shin, H.; Lee, H.N.; Ganesh, P.; Benali, A.; Kent, P.R.C.; et al. Doped NiO: The Mottness of a Charge Transfer Insulator. *Phys. Rev. B* **2020**, *101*, 195128. [[CrossRef](#)]
51. Luo, H.; Zhou, X.; Chen, Z.; Pei, Y.; Lu, X.; Wang, G. Fabrication and Characterization of High-Voltage NiO/β-Ga₂O₃ Heterojunction Power Diodes. *IEEE Trans. Electron Devices* **2021**, *68*, 3991–3996. [[CrossRef](#)]
52. Gong, H.; Chen, X.; Xu, Y.; Chen, Y.; Ren, F.; Liu, B.; Gu, S.; Zhang, R.; Ye, J. Band Alignment and Interface Recombination in NiO/β-Ga₂O₃ Type-II p-n Heterojunctions. *IEEE Trans. Electron Devices* **2020**, *67*, 3341–3347. [[CrossRef](#)]
53. Li, J.-S.; Wan, H.-H.; Chiang, C.-C.; Xia, X.; Yoo, T.J.; Kim, H.; Ren, F.; Pearton, S.J. Reproducible NiO/Ga₂O₃ Vertical Rectifiers with Breakdown Voltage >8 KV. *Crystals* **2023**, *13*, 886. [[CrossRef](#)]
54. Deng, Y.; Yang, Z.; Xu, T.; Jiang, H.; Ng, K.W.; Liao, C.; Su, D.; Pei, Y.; Chen, Z.; Wang, G.; et al. Band Alignment and Electrical Properties of NiO/β-Ga₂O₃ Heterojunctions with Different β-Ga₂O₃ Orientations. *Appl. Surf. Sci.* **2023**, *622*, 156917. [[CrossRef](#)]
55. Hao, W.; He, Q.; Zhou, K.; Xu, G.; Xiong, W.; Zhou, X.; Jian, G.; Chen, C.; Zhao, X.; Long, S. Low Defect Density and Small I–V Curve Hysteresis in NiO/β-Ga₂O₃ Pn Diode with a High PFOM of 0.65 GW/cm². *Appl. Phys. Lett.* **2021**, *118*, 043501. [[CrossRef](#)]
56. Yan, Q.; Gong, H.; Zhou, H.; Zhang, J.; Ye, J.; Liu, Z.; Wang, C.; Zheng, X.; Zhang, R.; Hao, Y. Low Density of Interface Trap States and Temperature Dependence Study of Ga₂O₃ Schottky Barrier Diode with P-NiOx Termination. *Appl. Phys. Lett.* **2022**, *120*, 092106. [[CrossRef](#)]
57. Li, J.-S.; Wan, H.-H.; Chiang, C.-C.; Ren, F.; Pearton, S.J. Annealing Stability of NiO/Ga₂O₃ Vertical Heterojunction Rectifiers. *Crystals* **2023**, *13*, 1174. [[CrossRef](#)]
58. Lu, X.; Zhou, X.; Jiang, H.; Ng, K.W.; Chen, Z.; Pei, Y.; Lau, K.M.; Wang, G. 1-KV Sputtered p-NiO/n-Ga₂O₃ Heterojunction Diodes with an Ultra-Low Leakage Current Below μA/cm². *IEEE Electron Device Lett.* **2020**, *41*, 449–452. [[CrossRef](#)]
59. Zhang, J.; Dong, P.; Dang, K.; Zhang, Y.; Yan, Q.; Xiang, H.; Su, J.; Liu, Z.; Si, M.; Gao, J.; et al. Ultra-Wide Bandgap Semiconductor Ga₂O₃ Power Diodes. *Nat. Commun.* **2022**, *13*, 3900. [[CrossRef](#)]
60. Chiang, C.-C.; Li, J.-S.; Wan, H.-H.; Ren, F.; Pearton, S.J. The Optimization of NiO Doping, Thickness, and Extension in KV-Class NiO/Ga₂O₃ Vertical Rectifiers. *Crystals* **2023**, *13*, 1124. [[CrossRef](#)]
61. Li, J.-S.; Chiang, C.-C.; Xia, X.; Wan, H.-H.; Ren, F.; Pearton, S.J. 1 Mm², 3.6 KV, 4.8 A NiO/Ga₂O₃ Heterojunction Rectifiers. *ECS J. Solid State Sci. Technol.* **2023**, *12*, 085001. [[CrossRef](#)]
62. Xiao, M.; Wang, B.; Spencer, J.; Qin, Y.; Porter, M.; Ma, Y.; Wang, Y.; Sasaki, K.; Tadjer, M.; Zhang, Y. NiO Junction Termination Extension for High-Voltage (>3 kV) Ga₂O₃ Devices. *Appl. Phys. Lett.* **2023**, *122*, 183501. [[CrossRef](#)]

63. Zhou, F.; Gong, H.H.; Wang, Z.P.; Xu, W.Z.; Yu, X.X.; Yang, Y.; Ren, F.-F.; Gu, S.L.; Zhang, R.; Zheng, Y.D.; et al. Over 1.8 GW/cm² Beveled-Mesa NiO/ β -Ga₂O₃ Heterojunction Diode with 800 V/10 A Nanosecond Switching Capability. *Appl. Phys. Lett.* **2021**, *119*, 262103. [\[CrossRef\]](#)
64. Hao, W.; He, Q.; Zhou, X.; Zhao, X.; Xu, G.; Long, S. 2.6 KV NiO/Ga₂O₃ Heterojunction Diode with Superior High-Temperature Voltage Blocking Capability. In Proceedings of the 2022 IEEE 34th International Symposium on Power Semiconductor Devices and ICs (ISPSD), Vancouver, BC, Canada, 22–25 May 2022; pp. 105–108.
65. Wang, Y.; Gong, H.; Lv, Y.; Fu, X.; Dun, S.; Han, T.; Liu, H.; Zhou, X.; Liang, S.; Ye, J.; et al. 2.41 KV Vertical P-NiO/n-Ga₂O₃ Heterojunction Diodes with a Record Baliga's Figure-of-Merit of 5.18 GW/cm². *IEEE Trans. Power Electron* **2022**, *37*, 3743–3746. [\[CrossRef\]](#)
66. Gong, H.H.; Chen, X.H.; Xu, Y.; Ren, F.-F.; Gu, S.L.; Ye, J.D. A 1.86-KV Double-Layered NiO/ β -Ga₂O₃ Vertical p–n Heterojunction Diode. *Appl. Phys. Lett.* **2020**, *117*, 022104. [\[CrossRef\]](#)
67. Li, J.-S.; Chiang, C.-C.; Xia, X.; Wan, H.-H.; Ren, F.; Pearton, S.J. 7.5 KV, 6.2 GW cm⁻² NiO/ β -Ga₂O₃ Vertical Rectifiers with on–off Ratio Greater than 10¹³. *J. Vac. Sci. Technol. A* **2023**, *41*, 030401. [\[CrossRef\]](#)
68. Wang, B.; Xiao, M.; Spencer, J.; Qin, Y.; Sasaki, K.; Tadjer, M.J.; Zhang, Y. 2.5 KV Vertical Ga₂O₃ Schottky Rectifier with Graded Junction Termination Extension. *IEEE Electron Device Lett.* **2023**, *44*, 221–224. [\[CrossRef\]](#)
69. Gong, H.H.; Yu, X.X.; Xu, Y.; Chen, X.H.; Kuang, Y.; Lv, Y.J.; Yang, Y.; Ren, F.-F.; Feng, Z.H.; Gu, S.L.; et al. β -Ga₂O₃ Vertical Heterojunction Barrier Schottky Diodes Terminated with p-NiO Field Limiting Rings. *Appl. Phys. Lett.* **2021**, *118*, 202102. [\[CrossRef\]](#)
70. Wang, Y.; Gong, H.; Jia, X.; Han, G.; Ye, J.; Liu, Y.; Hu, H.; Ou, X.; Ma, X.; Hao, Y. First Demonstration of RESURF and Superjunction β -Ga₂O₃ MOSFETs with p-NiO/n-Ga₂O₃ Junctions. In Proceedings of the 2021 IEEE International Electron Devices Meeting (IEDM), San Francisco, CA, USA, 11–16 December 2021; pp. 36.6.1–36.6.4.
71. Qin, Y.; Xiao, M.; Porter, M.; Ma, Y.; Spencer, J.; Du, Z.; Jacobs, A.G.; Sasaki, K.; Wang, H.; Tadjer, M.; et al. 10-KV Ga₂O₃ Charge-Balance Schottky Rectifier Operational at 200 °C. *IEEE Electron Device Lett.* **2023**, *44*, 1268–1271. [\[CrossRef\]](#)
72. Lv, Y.; Wang, Y.; Fu, X.; Dun, S.; Sun, Z.; Liu, H.; Zhou, X.; Song, X.; Dang, K.; Liang, S.; et al. Demonstration of β -Ga₂O₃ Junction Barrier Schottky Diodes with a Baliga's Figure of Merit of 0.85 GW/cm² or a 5A/700 V Handling Capabilities. *IEEE Trans. Power Electron* **2021**, *36*, 6179–6182. [\[CrossRef\]](#)
73. Yan, Q.; Gong, H.; Zhang, J.; Ye, J.; Zhou, H.; Liu, Z.; Xu, S.; Wang, C.; Hu, Z.; Feng, Q.; et al. β -Ga₂O₃ Hetero-Junction Barrier Schottky Diode with Reverse Leakage Current Modulation and BV²/Ron,Sp Value of 0.93 GW/cm². *Appl. Phys. Lett.* **2021**, *118*, 122102. [\[CrossRef\]](#)
74. Wu, F.; Wang, Y.; Jian, G.; Xu, G.; Zhou, X.; Guo, W.; Du, J.; Liu, Q.; Dun, S.; Yu, Z.; et al. Superior Performance β -Ga₂O₃ Junction Barrier Schottky Diodes Implementing p-NiO Heterojunction and Beveled Field Plate for Hybrid Cockcroft–Walton Voltage Multiplier. *IEEE Trans. Electron Devices* **2023**, *70*, 1199–1205. [\[CrossRef\]](#)
75. Wang, C.; Gong, H.; Lei, W.; Cai, Y.; Hu, Z.; Xu, S.; Liu, Z.; Feng, Q.; Zhou, H.; Ye, J.; et al. Demonstration of the P-NiO_x/n-Ga₂O₃ Heterojunction Gate FETs and Diodes with BV²/R_{on,Sp} Figures of Merit of 0.39 GW/cm² and 1.38 GW/cm². *IEEE Electron Device Lett.* **2021**, *42*, 485–488. [\[CrossRef\]](#)
76. Zhou, X.; Liu, Q.; Hao, W.; Xu, G.; Long, S. Normally-off β -Ga₂O₃ Power Heterojunction Field-Effect-Transistor Realized by p-NiO and Recessed-Gate. In Proceedings of the 2022 IEEE 34th International Symposium on Power Semiconductor Devices and ICs (ISPSD), Vancouver, BC, Canada, 22–25 May 2022; pp. 101–104.
77. Ashwin Kumar Saikumar, S.D.N.; Sundaram, K.B. A Review of Recent Developments in Aluminum Gallium Oxide Thin Films and Devices. *Crit. Rev. Solid State Mater. Sci.* **2022**, *47*, 538–569. [\[CrossRef\]](#)
78. Ranga, P.; Rishinaramangalam, A.; Varley, J.; Bhattacharyya, A.; Feezell, D.; Krishnamoorthy, S. Si-Doped β -(Al_{0.26}Ga_{0.74})₂O₃ Thin Films and Heterostructures Grown by Metalorganic Vapor-Phase Epitaxy. *Appl. Phys. Express* **2019**, *12*, 111004. [\[CrossRef\]](#)
79. Okumura, H.; Kato, Y.; Oshima, T.; Palacios, T. Demonstration of Lateral Field-Effect Transistors Using Sn-Doped β -(AlGa)₂O₃ (010). *Jpn. J. Appl. Phys.* **2019**, *58*, SBBD12. [\[CrossRef\]](#)
80. Peelaers, H.; Varley, J.B.; Speck, J.S.; Van de Walle, C.G. Structural and electronic properties of Ga₂O₃-Al₂O₃ alloys. *Appl. Phys. Lett.* **2018**, *112*, 242101. [\[CrossRef\]](#)
81. Zhang, F.; Saito, K.; Tanaka, T.; Nishio, M.; Arita, M.; Guo, Q. Wide Bandgap Engineering of (AlGa)₂O₃ Films. *Appl. Phys. Lett.* **2014**, *105*, 162107. [\[CrossRef\]](#)
82. Wang, C.-C.; Yuan, S.-H.; Ou, S.-L.; Huang, S.-Y.; Lin, K.-Y.; Chen, Y.-A.; Hsiao, P.-W.; Wu, D.-S. Growth and Characterization of Co-Sputtered Aluminum-Gallium Oxide Thin Films on Sapphire Substrates. *J. Alloys Compd.* **2018**, *765*, 894–900. [\[CrossRef\]](#)
83. Oshima, T.; Okuno, T.; Arai, N.; Kobayashi, Y.; Fujita, S. β -Al_{2x}Ga_{2-2x}O₃ Thin Film Growth by Molecular Beam Epitaxy. *Jpn. J. Appl. Phys.* **2009**, *48*, 070202. [\[CrossRef\]](#)
84. Oshima, Y.; Ahmadi, E.; Badescu, S.C.; Wu, F.; Speck, J.S. Composition Determination of β -(Al_xGa_{1-x})₂O₃ Layers Coherently Grown on (010) β -Ga₂O₃ Substrates by High-Resolution X-Ray Diffraction. *Appl. Phys. Express* **2016**, *9*, 061102. [\[CrossRef\]](#)
85. Kaun, S.W.; Wu, F.; Speck, J.S. β -(Al_xGa_{1-x})₂O₃/Ga₂O₃ (010) Heterostructures Grown on β -Ga₂O₃ (010) Substrates by Plasma-Assisted Molecular Beam Epitaxy. *J. Vac. Sci. Technol. A* **2015**, *33*, 041508. [\[CrossRef\]](#)
86. Zhang, Y.; Neal, A.; Xia, Z.; Joishi, C.; Johnson, J.M.; Zheng, Y.; Bajaj, S.; Brenner, M.; Dorsey, D.; Chabak, K.; et al. Demonstration of High Mobility and Quantum Transport in Modulation-Doped β -(Al_xGa_{1-x})₂O₃/Ga₂O₃ Heterostructures. *Appl. Phys. Lett.* **2018**, *112*, 173502. [\[CrossRef\]](#)
87. Miller, R.; Alema, F.; Osinsky, A. Epitaxial β -Ga₂O₃ and β -(Al_xGa_{1-x})₂O₃/ β -Ga₂O₃ Heterostructures Growth for Power Electronics. *IEEE Trans. Semicond. Manuf.* **2018**, *31*, 467–474. [\[CrossRef\]](#)

88. Zhang, Y.; Mauze, A.; Speck, J.S. *Development of β -(Al_xGa_{1-x})₂O₃/Ga₂O₃ Heterostructures*; University of California: Santa Barbara CA, USA, 2019.
89. Bhuiyan, A.F.M.A.U.; Meng, L.; Huang, H.-L.; Chae, C.; Hwang, J.; Zhao, H. Al Incorporation up to 99% in Metalorganic Chemical Vapor Deposition-Grown Monoclinic (Al_xGa_{1-x})₂O₃ Films Using Trimethylgallium. *Phys. Status Solidi (RRL)–Rapid Res. Lett.* **2023**, *17*, 2300224. [[CrossRef](#)]
90. Wang, D.; Mudiyansele, D.H.; Fu, H. Design Space of Delta-Doped β -(Al_xGa_{1-x})₂O₃/Ga₂O₃ High-Electron Mobility Transistors. *IEEE Trans. Electron Devices* **2022**, *69*, 69–74. [[CrossRef](#)]
91. Ahmadi, E.; Koksaldi, O.S.; Zheng, X.; Mates, T.; Oshima, Y.; Mishra, U.K.; Speck, J.S. Demonstration of β -(Al_xGa_{1-x})₂O₃/ β -Ga₂O₃ Modulation Doped Field-Effect Transistors with Ge as Dopant Grown via Plasma-Assisted Molecular Beam Epitaxy. *Appl. Phys. Express* **2017**, *10*, 071101. [[CrossRef](#)]
92. Kalarickal, N.K.; Xia, Z.; McGlone, J.F.; Liu, Y.; Moore, W.; Arehart, A.R.; Ringel, S.A.; Rajan, S. High Electron Density β -(Al_{0.17}Ga_{0.83})₂O₃/Ga₂O₃ Modulation Doping Using an Ultra-Thin (1 Nm) Spacer Layer. *J. Appl. Phys.* **2020**, *127*, 215706. [[CrossRef](#)]
93. Kalarickal, N.K.; Feng, Z.; Anhar Uddin Bhuiyan, A.F.M.; Xia, Z.; Moore, W.; McGlone, J.F.; Arehart, A.R.; Ringel, S.A.; Zhao, H.; Rajan, S. Electrostatic Engineering Using Extreme Permittivity Materials for Ultra-Wide Bandgap Semiconductor Transistors. *IEEE Trans. Electron Devices* **2021**, *68*, 29–35. [[CrossRef](#)]
94. Zhang, Y.; Joishi, C.; Xia, Z.; Brenner, M.; Lodha, S.; Rajan, S. Demonstration of β -(Al_xGa_{1-x})₂O₃/Ga₂O₃ Double Heterostructure Field Effect Transistors. *Appl. Phys. Lett.* **2018**, *112*, 233503. [[CrossRef](#)]
95. Kalarickal, N.K.; Xia, Z.; Huang, H.-L.; Moore, W.; Liu, Y.; Brenner, M.; Hwang, J.; Rajan, S. β -(Al_{0.18}Ga_{0.82})₂O₃/Ga₂O₃ Double Heterojunction Transistor with Average Field of 5.5 MV/Cm. *IEEE Electron Device Lett.* **2021**, *42*, 899–902. [[CrossRef](#)]
96. Vaidya, A.; Saha, C.N.; Singiseti, U. Enhancement Mode β -(Al_xGa_{1-x})₂O₃/Ga₂O₃ Heterostructure FET (HFET) with High Transconductance and Cutoff Frequency. *IEEE Electron Device Lett.* **2021**, *42*, 1444–1447. [[CrossRef](#)]
97. Joishi, C.; Zhang, Y.; Xia, Z.; Sun, W.; Arehart, A.R.; Ringel, S.; Lodha, S.; Rajan, S. Breakdown Characteristics of β -(Al_{0.22}Ga_{0.78})₂O₃/Ga₂O₃ Field-Plated Modulation-Doped Field-Effect Transistors. *IEEE Electron Device Lett.* **2019**, *40*, 1241–1244. [[CrossRef](#)]
98. Wang, D.; Mudiyansele, D.H.; Fu, H. Design of KV-Class and Low RON E-Mode β -Ga₂O₃ Current Aperture Vertical Transistors with Delta-Doped β -(Al_xGa_{1-x})₂O₃/Ga₂O₃ Heterostructure. *IEEE Trans. Electron Devices* **2023**, *70*, 5795–5802. [[CrossRef](#)]
99. Sundaram, P.P.; Alema, F.; Osinsky, A.; Koester, S.J. β -(Al_xGa_{1-x})₂O₃/Ga₂O₃ Heterostructure Schottky Diodes for Improved VBR2/RON. *J. Vac. Sci. Technol. A* **2022**, *40*, 043211. [[CrossRef](#)]
100. Ahmadi, E.; Oshima, Y.; Wu, F.; Speck, J.S. Schottky Barrier Height of Ni to β -(Al_xGa_{1-x})₂O₃ with Different Compositions Grown by Plasma-Assisted Molecular Beam Epitaxy. *Semicond. Sci. Technol.* **2017**, *32*, 035004. [[CrossRef](#)]
101. Mudiyansele, D.H.; Wang, D.; Fu, H. Ultrawide Bandgap Vertical β -(Al_xGa_{1-x})₂O₃ Schottky Barrier Diodes on Free-Standing β -Ga₂O₃ Substrates. *J. Vac. Sci. Technol. A* **2023**, *41*, 023201. [[CrossRef](#)]
102. Wan, H.-H.; Li, J.-S.; Chiang, C.-C.; Xia, X.; Ren, F.; Masten, H.N.; Lundh, J.S.; Spencer, J.A.; Alema, F.; Osinsky, A.; et al. Operation of NiO/ β -(Al_{0.21}Ga_{0.79})₂O₃/Ga₂O₃ Heterojunction Lateral Rectifiers at up to 225 °C. *ECS J. Solid State Sci. Technol.* **2023**, *12*, 075008. [[CrossRef](#)]
103. Wan, H.-H.; Li, J.-S.; Chiang, C.-C.; Xia, X.; Ren, F.; Masten, H.N.; Lundh, J.S.; Spencer, J.A.; Alema, F.; Osinsky, A.; et al. NiO/ β -(Al_xGa_{1-x})₂O₃/Ga₂O₃ Heterojunction Lateral Rectifiers with Reverse Breakdown Voltage >7 kV. *J. Vac. Sci. Technol. A* **2023**, *41*, 032701. [[CrossRef](#)]
104. Montes, J.; Yang, C.; Fu, H.; Yang, T.-H.; Fu, K.; Chen, H.; Zhou, J.; Huang, X.; Zhao, Y. Demonstration of Mechanically Exfoliated β -Ga₂O₃/GaN p-n Heterojunction. *Appl. Phys. Lett.* **2019**, *114*, 162103. [[CrossRef](#)]
105. Herath Mudiyansele, D.; Wang, D.; Fu, H. Wide Bandgap Vertical KV-Class β -Ga₂O₃/GaN Heterojunction p-n Power Diodes with Mesa Edge Termination. *IEEE J. Electron Devices Soc.* **2022**, *10*, 89–97. [[CrossRef](#)]
106. Nandi, A.; Rana, K.S.; Bag, A. Design and Analysis of P-GaN/N-Ga₂O₃ Based Junction Barrier Schottky Diodes. *IEEE Trans. Electron Devices* **2021**, *68*, 6052–6058. [[CrossRef](#)]
107. Mudiyansele, D.H.; Wang, D.; Fu, H. Design and Analysis of KV-Class Ultrawide Bandgap β -Ga₂O₃/p-GaN Heterojunction Barrier Schottky Diodes. In Proceedings of the 2022 Compound Semiconductor Week (CSW), Ann Arbor, MI, USA, 1–3 June 2022; pp. 1–2.
108. Nakagomi, S.; Momo, T.; Takahashi, S.; Kokubun, Y. Deep Ultraviolet Photodiodes Based on β -Ga₂O₃/SiC Heterojunction. *Appl. Phys. Lett.* **2013**, *103*, 072105. [[CrossRef](#)]
109. Nakagomi, S.; Hiratsuka, K.; Kakuda, Y.; Yoshihiro, K. Beta-Gallium Oxide/SiC Heterojunction Diodes with High Rectification Ratios. *ECS J. Solid State Sci. Technol.* **2016**, *6*, Q3030. [[CrossRef](#)]
110. Song, Y.; Bhattacharyya, A.; Karim, A.; Shoemaker, D.; Huang, H.-L.; Roy, S.; McGray, C.; Leach, J.H.; Hwang, J.; Krishnamoorthy, S.; et al. Ultra-Wide Band Gap Ga₂O₃-on-SiC MOSFETs. *ACS Appl. Mater. Interfaces* **2023**, *15*, 7137–7147. [[CrossRef](#)]
111. Watahiki, T.; Yuda, Y.; Furukawa, A.; Yamamuka, M.; Takiguchi, Y.; Miyajima, S. Heterojunction P-Cu₂O/n-Ga₂O₃ Diode with High Breakdown Voltage. *Appl. Phys. Lett.* **2017**, *111*, 222104. [[CrossRef](#)]
112. Gallagher, J.C.; Koehler, A.D.; Tadjer, M.J.; Mahadik, N.A.; Anderson, T.J.; Budhathoki, S.; Law, K.-M.; Hauser, A.J.; Hobart, K.D.; Kub, F.J. Demonstration of CuI as a P-N Heterojunction to β -Ga₂O₃. *Appl. Phys. Express* **2019**, *12*, 104005. [[CrossRef](#)]
113. Budde, M.; Splith, D.; Mazzolini, P.; Tahraoui, A.; Feldl, J.; Ramsteiner, M.; von Wenckstern, H.; Grundmann, M.; Bierwagen, O. SnO/ β -Ga₂O₃ Vertical Pn Heterojunction Diodes. *Appl. Phys. Lett.* **2020**, *117*, 252106. [[CrossRef](#)]
114. Tetzner, K.; Egbo, K.; Klupsch, M.; Unger, R.-S.; Popp, A.; Chou, T.-S.; Anooz, S.B.; Galazka, Z.; Trampert, A.; Bierwagen, O.; et al. SnO/ β -Ga₂O₃ Heterojunction Field-Effect Transistors and Vertical p-n Diodes. *Appl. Phys. Lett.* **2022**, *120*, 112110. [[CrossRef](#)]

115. Umezawa, H. Recent Advances in Diamond Power Semiconductor Devices. *Mater. Sci. Semicond. Process* **2018**, *78*, 147–156. [[CrossRef](#)]
116. Isberg, J.; Hammersberg, J.; Johansson, E.; Wikström, T.; Twitchen, D.J.; Whitehead, A.J.; Coe, S.E.; Scarsbrook, G.A. High Carrier Mobility in Single-Crystal Plasma-Deposited Diamond. *Science* **2002**, *297*, 1670–1672. [[CrossRef](#)] [[PubMed](#)]
117. Sittimart, P.; Ohmagari, S.; Matsumae, T.; Umezawa, H.; Yoshitake, T. Diamond/ β -Ga₂O₃ Pn Heterojunction Diodes Fabricated by Low-Temperature Direct-Bonding. *AIP Adv.* **2021**, *11*, 105114. [[CrossRef](#)]
118. Matsumae, T.; Kurashima, Y.; Umezawa, H.; Tanaka, K.; Ito, T.; Watanabe, H.; Takagi, H. Low-Temperature Direct Bonding of β -Ga₂O₃ and Diamond Substrates under Atmospheric Conditions. *Appl. Phys. Lett.* **2020**, *116*, 141602. [[CrossRef](#)]
119. Nandi, A.; Cherns, D.; Sanyal, I.; Kuball, M. Epitaxial Growth of (−201) β -Ga₂O₃ on (001) Diamond Substrates. *Cryst. Growth Des.* **2023**, *23*, 8290–8295. [[CrossRef](#)] [[PubMed](#)]
120. Kusaba, T.; Sittimart, P.; Katamune, Y.; Kageura, T.; Naragino, H.; Ohmagari, S.; Valappil, S.M.; Nagano, S.; Zkria, A.; Yoshitake, T. Heteroepitaxial Growth of β -Ga₂O₃ Thin Films on Single Crystalline Diamond (111) Substrates by Radio Frequency Magnetron Sputtering. *Appl. Phys. Express* **2023**, *16*, 105503. [[CrossRef](#)]
121. Mishra, A.; Abdallah, Z.; Pomeroy, J.W.; Uren, M.J.; Kuball, M. Electrical and Thermal Performance of Ga₂O₃–Al₂O₃–Diamond Super-Junction Schottky Barrier Diodes. *IEEE Trans. Electron Devices* **2021**, *68*, 5055–5061. [[CrossRef](#)]
122. Malakoutian, M.; Song, Y.; Yuan, C.; Ren, C.; Lundh, J.S.; Lavelle, R.M.; Brown, J.E.; Snyder, D.W.; Graham, S.; Choi, S.; et al. Polycrystalline Diamond Growth on β -Ga₂O₃ for Thermal Management. *Appl. Phys. Express* **2021**, *14*, 55502. [[CrossRef](#)]
123. Rahaman, I.; Ellis, H.D.; Fu, K. Robust Diamond/ β -Ga₂O₃ Hetero-p-n-Junction Via Mechanically Integrating Their Building Blocks. *arXiv* **2023**, arXiv:2311.16323.
124. Hickman, A.L.; Chaudhuri, R.; Bader, S.J.; Nomoto, K.; Li, L.; Hwang, J.C.M.; Xing, H.G.; Jena, D. Next Generation Electronics on the Ultrawide-Bandgap Aluminum Nitride Platform. *Semicond. Sci. Technol.* **2021**, *36*, 44001. [[CrossRef](#)]
125. Chen, J.-X.; Tao, J.-J.; Ma, H.-P.; Zhang, H.; Feng, J.-J.; Liu, W.-J.; Xia, C.; Lu, H.-L.; Zhang, D.W. Band Alignment of AlN/ β -Ga₂O₃ Heterojunction Interface Measured by x-Ray Photoelectron Spectroscopy. *Appl. Phys. Lett.* **2018**, *112*, 261602. [[CrossRef](#)]
126. Song, K.; Zhang, H.; Fu, H.; Yang, C.; Singh, R.; Zhao, Y.; Sun, H.; Long, S. Normally-off AlN/ β -Ga₂O₃ Field-Effect Transistors Using Polarization-Induced Doping. *J. Phys. D Appl. Phys.* **2020**, *53*, 345107. [[CrossRef](#)]
127. Baskaran, S.; Shunmugathammal, M.; Sivamani, C.; Ravi, S.; Murugapandiyar, P.; Ramkumar, N. UWBG AlN/ β -Ga₂O₃ HEMT on Silicon Carbide Substrate for Low Loss Portable Power Converters and RF Applications. *Silicon* **2022**, *14*, 11079–11087. [[CrossRef](#)]
128. He, Z.; Fu, K.; Xu, M.; Zhou, J.; Li, T.; Zhao, Y. Understanding the Breakdown Behavior of Ultrawide-Bandgap Boron Nitride Power Diodes Using Device Modeling. *Phys. Status Solidi (RRL)–Rapid Res. Lett.* **2023**, 2200397. [[CrossRef](#)]
129. Biswas, A.; Xu, M.; Fu, K.; Zhou, J.; Xu, R.; Puthirath, A.B.; Hachtel, J.A.; Li, C.; Iyengar, S.A.; Kannan, H.; et al. Properties and Device Performance of BN Thin Films Grown on GaN by Pulsed Laser Deposition. *Appl. Phys. Lett.* **2022**, *121*, 092105. [[CrossRef](#)]
130. Xu, M.; Biswas, A.; Li, T.; He, Z.; Luo, S.; Mei, Z.; Zhou, J.; Chang, C.; Puthirath, A.B.; Vajtai, R.; et al. Vertical β -Ga₂O₃ Metal–Insulator–Semiconductor Diodes with an Ultrathin Boron Nitride Interlayer. *Appl. Phys. Lett.* **2023**, *123*, 232107. [[CrossRef](#)]
131. Lemme, M.C.; Akinwande, D.; Huyghebaert, C.; Stampfer, C. 2D Materials for Future Heterogeneous Electronics. *Nat. Commun.* **2022**, *13*, 1392. [[CrossRef](#)]
132. Su, S.-K.; Chuu, C.-P.; Li, M.-Y.; Cheng, C.-C.; Wong, H.-S.P.; Li, L.-J. Layered Semiconducting 2D Materials for Future Transistor Applications. *Small Struct.* **2021**, *2*, 2000103. [[CrossRef](#)]
133. Yan, X.; Esqueda, I.S.; Ma, J.; Tice, J.; Wang, H. High Breakdown Electric Field in β -Ga₂O₃/Graphene Vertical Barrier Heterostructure. *Appl. Phys. Lett.* **2018**, *112*, 032101. [[CrossRef](#)]
134. Kim, J.; Mastro, M.A.; Tadjer, M.J.; Kim, J. Heterostructure WSe₂–Ga₂O₃ Junction Field-Effect Transistor for Low-Dimensional High-Power Electronics. *ACS Appl. Mater. Interfaces* **2018**, *10*, 29724–29729. [[CrossRef](#)] [[PubMed](#)]
135. Leblanc, C.; Herath Mudiyanse, D.; Song, S.; Zhang, H.; Davydov, A.V.; Fu, H.; Jariwala, D. Vertical van Der Waals Heterojunction Diodes Comprising 2D Semiconductors on 3D β -Ga₂O₃. *Nanoscale* **2023**, *15*, 9964–9972. [[CrossRef](#)] [[PubMed](#)]

Disclaimer/Publisher’s Note: The statements, opinions and data contained in all publications are solely those of the individual author(s) and contributor(s) and not of MDPI and/or the editor(s). MDPI and/or the editor(s) disclaim responsibility for any injury to people or property resulting from any ideas, methods, instructions or products referred to in the content.